FYS-3931

Master's Thesis in Space Physics

A theoretical study of the coupling between minor ions and protons in the solar transition region

Hanne Sigrun Byhring

June, 2007

Faculty of Science

Department of Physics and Technology

University of Tromsø

Forord

Aller først må jeg takke min veileder, Ruth Esser, for all hjelp og støtte, og for at hun har gitt meg en veldig spennende og morsom oppgave å jobbe med! Pappaen min pleier å si at livet er som en sykkeltur, med slitsomme oppoverbakker, vakker utsikt fra toppene og herlige nedoverbakker der det kiler i magen. Å skrive masteroppgave er også litt som en sykkeltur. Av Ruth har jeg fått sykkel, kart, og et puff i baken i de tyngste kneikene. For det er jeg meget takknemmlig. Dernest vil jeg takke alle studenter og ansatte ved Institutt for Teoretisk Astrofysikk ved Universitetet i Oslo, som har vært så gjestfrie og tatt så godt imot meg. Her må spesielt nevnes Egil Leer og studentene i AFU som sørget for at jeg fikk en lesesalsplass nede i "Stjernekjelleren" mens jeg jobbet med denne oppgaven. Der har jeg hatt det utrolig koselig! En stor takk fortjener også Øystein Lie-Svendsen, som hjalp meg med noen rettelser helt på tampen, og selvfølgelig min kjære Magnar, som har lest gjennom oppgaven for meg og kommet med mange nyttige kommentarer. Sist, men ikke minst, vil jeg takke familie og venner, som har støttet meg, skrytt av meg, gjort meg modig og trodd på meg gjennom hele utdannelsen min!

Abstract

We have used a numerical model to calculate the flow velocities of six minor ion species, using two different background models for the fast solar wind, one with a slow expansion, and one with a very rapidly expanding geometry. By comparing the flow velocity of the minor ions and the protons, we have investigated the degree of coupling between minor ions and the background solar wind in the solar transition region.

We find that $C^{3+}, O^{3+}, O^{4+}, O^{5+}$ and Ne^{7+} are well coupled to the protons in the transition region, for both background models. These ions have well defined ion fraction maxima, and the region of maximum ion fraction corresponds to a narrow height range. These results show that observations of the Doppler-shift of the ionic emission lines from these ions reflect the outflow velocity of the background solar wind in the transition region quite well.

The Mg^{8+} ion fraction has no well defined maximum, and the radiation from this ion may stem from an extended height region. The region where Mg^{8+} is a dominant charge state of magnesium includes regions of very high outflow. The significance of the contribution from regions of high outflow, to the total Doppler-shift of the Mg IX emission line, can be determined through a calculation of the spectral emission profile.

We have also compared the calculated outflow velocities with observations from ten different authors. There are significant discrepancies between calculated outflow velocities, and observations, for several minor ions, in both background models. For the ions of carbon and oxygen that we have considered, the flow velocity in the background model with a very rapid expansion, are too high compared with observations. The flow velocity of these ions in the slowly expanding geometry is very low, and in better accordance with the observations. For Ne^{7+}, the flow velocity is relatively low compared to observations for both background models, however, it is a little higher in the rapidly expanding geometry. We find that these discrepancies cannot be resolved by changing the heating of the minor ions without increasing the heating rates to very large values. Our results also indicate that large heating rates lead to a high abundance of low charge states in the solar wind. This is not consistent with observations of charge state densities in-situ. We believe that a background model with an intermediate expansion

might provide a better fit to the observations.

Finally, we have compared the formation temperatures obtained in the simulations with the formation temperatures obtained when assuming ionization equilibrium. We find that for the background model with a slowly expanding geometry, the formation temperatures do not deviate significantly from ionization equilibrium. For the rapidly expanding geometry, the deviation from ionization equilibrium is significant for all the ions, with a maximum shift in formation temperature of $4.3 \cdot 10^5$ K, for O^{5+}. For Mg^{8+} a formation temperature cannot be defined in either of the background models, because, as mentioned above, the ion fraction has no well defined maximum.

Contents

Chapter 1

Introduction

The acceleration of the solar wind has been a topic of research since before the solar wind was observed for the first time (*Neugebauer and Snyder*, 1966, and references therein). In spite of this,much still remains to be done before we can claim a thorough understanding of the processes that provide the energy for the acceleration of the solar wind, and for the heating of the corona.

Much of the solar wind research has concentrated on the fast solar wind. This because it is less structured, less variable and presumably less complicated than the slow solar wind. The density in the coronal holes, where the fast solar wind has its origin (e.g. *Bell and Noci*, 1976), is lower than the density in the source region of the slow solar wind, which is believed to lie in the surrounding regions, and during solar minimum, mainly in the streamer belt in the equatorial regions of the sun (e.g. *Gosling*, 1997). Since the density in coronal holes is low, it is believed that the plasma in coronal holes is dominated by collissionless processes, such as wave-particle interactions. These processes will manifest themselves in the particle velocity distributions. In a collision dominated solar wind plasma, traces in the particle velocity distributions, of collisionless processes in the corona, will disappear before we are able to detect them. However, if the plasma is collisionless all the way from the corona to the spacecraft, the traces of collisionless processes in the corona can be detected. Since collisionless processes are believed to be important in the acceleration of the solar wind (*Cranmer*, 2004, and references therein), studies of the fast solar wind, where the effects of collisionless processes can be detected, are particularly important (*Hollweg*, 2006).

In chapter 2 we shall present some basic properties of the fast solar wind from coronal holes, as well as a short review of the source regions and some of the proposed acceleration mechanisms of the fast solar wind.

One of the essential questions is at what heights in the solar atmosphere the fast solar wind begins to pick up speed. This question is important for

the understanding of the acceleration mechanism of the solar wind as well as for determining the source regions of the fast solar wind inside coronal holes.

Several authors have estimated flow velocities in the transition region and lower corona from observations of ionic spectral lines in coronal holes. A summary of some of these observations is presented in chapter 3.

The aim of this study, is to compare calculated outflow velocities of minor ions and protons, using a numerical model (*Hansteen and Leer*, 1995; *Lie-Svendsen et al.*, 2001) based on a newly developed set of gyrotropic transport equations (*Janse et al.*, 2005), to obtain an indication of whether it is reasonable to assume that the observed minor ion outflow velocities in the transition region represent the outflow velocity of the background proton-electron solar wind. We also wish to compare calculated with observed minor ion outflow velocities in the transition region, and calculated minor ion formation temperatures with the formation temperatures obtained by assuming ionization equilibrium. If the outflow velocity in the formation region of these ions is large, they may not be in ionization equilibrium, and consequently, the source region of the ionic emission lines may be moved to higher temperatures, i.e. altitudes, in the solar atmosphere. If observed minor ion outflow velocities are to be used as constraints on the background solar wind it is equally important to know where the source regions of the ionic emission lines are, as to know that these ions are in fact well coupled to the background.

The choice of minor ions for the simulations is based on the availability of observational results.

Chapter 2

The fast solar wind

To better understand the motive for this study it may be helpful to review some of the history of solar wind research. In this chapter we will first present a very brief overview of the temperature-structure of the solar atmosphere, as well as some properties of the fast solar wind. We will then describe three physical mechanisms proposed as the drivers of the fast solar wind. Finally, we shall briefly review what is known about the coronal source regions of the fast solar wind.

2.1 The solar atmosphere

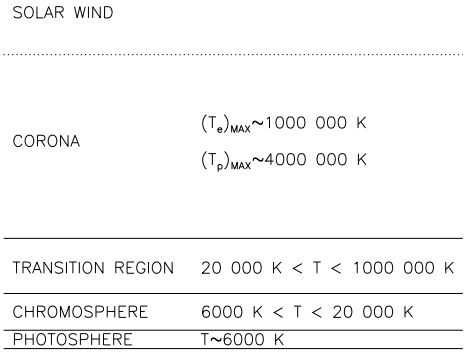

Figure 2.1: Schematic of the temperature structure of the solar atmosphere, the depth of the layers is not correctly scaled.

A schematic figure of the structure of the solar atmosphere is shown in figure 2.1. The photosphere is usually thought of as the surface of the sun. It holds a temperature of about 6000 K, and is the source of the continuous part of the solar spectrum (i.e. black body radiation). Owing to the relatively low temperature of the photosphere, compared to the solar interior and the outer layers of the solar atmosphere, it is dominated by neutral hydrogen gas. Minor ions are also mostly in the neutral state here. Above the photosphere is the chromosphere, where the temperature lies between 6000 K and about 20 000 K.

The chromosphere is also mostly dominated by neutral hydrogen gas, but in the upper layers of the chromosphere, ionization of both hydrogen and minor ions begins. The next layer of the solar atmosphere is called the transition region, where the temperature increases from $2 \cdot 10^4$ K to about $1 \cdot 10^6$ K, over a very narrow height region. Here, both hydrogen and minor ions become ionized, although many minor ions are not fully ionized, even in the corona. The uppermost layer of the solar atmosphere, which also stretches into interplanetary space, where it is named the solar wind, is the corona. In the corona we find the temperature maximum in the solar atmosphere, with an electron temperature of about $1 \cdot 10^6$ K and proton temperatures of $2 - 4 \cdot 10^6$ K (see also next section).

2.2 Properties of the fast solar wind

In the literature, the solar wind is usually divided into two categories, fast and slow solar wind. The distinction is made, as is reflected in the names "fast" and "slow", on the basis of the measured velocity of the solar wind particles in interplanetary space. The velocity of the solar wind is highly variable, and it can be difficult to distinguish between the two types. The wind is usually called "slow" if the average velocity over some time is below 500 km/s (at exactly what velocity the distinction is made varies somewhat between different authors), and "fast" if the average velocity exceeds 500 km/s for a substantial period of time. The fast wind usually has a higher average temperature than the slow wind (e.g. *Burlaga and Ogilvie*, 1970; *Lopez and Freeman*, 1986). The average proton temperature in the fast solar wind at earth orbit (1 AU) is about $2.3 \cdot 10^5$ K (*Schwenn*, 1990). The proton density in the solar wind is anti-correlated with the solar wind speed, in fact the mass flux of the solar wind is more or less constant (e.g. *Steinitz and Eyni*, 1980; *Neugebauer and Snyder*, 1966). The average proton density in the fast solar wind at 1 AU is about 2.73 cm^{-3} (*Schwenn*, 1990). The properties of the fast solar wind from large long-lived coronal holes are relatively constant. The largest coronal holes are found in the polar regions of the sun around solar minimum, and smaller ones occasionally also occur in the equatorial regions of the sun, particularly around solar maximum (e.g. *Miralles et al.*, 2001).

In figures 2.2-2.4 we have plotted some properties of the fast solar wind from polar coronal holes, in the region close to the sun. Figure 2.2 shows observed electron temperatures in the range from 1-1.6$R_\odot$ (where $R_\odot$ is the solar radius). They vary between about $3 \cdot 10^5$ and $1.2 \cdot 10^6$ K. The horizontal lines indicate a temperature range (*Wilhelm et al.*, 1998), or the height range associated with an observed electron temperature (*Wilhelm*, 2006). Protons and hydrogen are expected to be strongly coupled in the corona, and the hydrogen temperature here should also reflect the proton

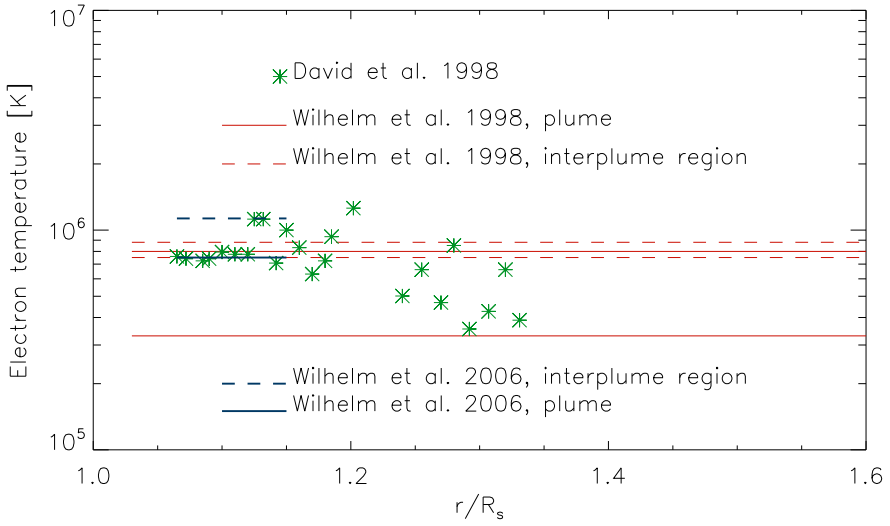

Figure 2.2: Observed electron temperatures in coronal holes plotted vs. radial distance from the solar center. For a short description of plumes/interplume regions, see section 2.4.2

temperature. Hydrogen temperatures can be deduced from observations of the width of the emission line produced by the coronal hydrogen population. *Kohl et al.* (1997) find a temperature of about $2{\cdot}10^6$K at $1.5R_\odot$. *Esser et al.* (1999) find temperatures between $2{\cdot}10^6$ K and $3{\cdot}10^6$ K in the height region 1.5-2.5$R_\odot$. *Cranmer et al.* (1999) find a temperature of $2.2{\cdot}10^6$ K at $1.5R_\odot$ and $3.5{\cdot}10^6$ K at $2.5R_\odot$.

The density in polar coronal holes (figure 2.3) decreases rapidly from about 10^{14} to $10^{11}m^{-3}$ between $1R_\odot$ and $3R_\odot$. Using the conservation of mass, and the observed densities of, e.g. *Guhathakurta et al.* (1996), we can calculate the proton (and electron) outflow velocity for a given magnetic field geometry. We have assumed spherical symmetry. The result is shown in figure 2.4. Also shown are outflow velocities for hydrogen, and for O^{5+}, deduced from observations of Doppler dimming/pumping of the oxygen O VI 1032 and O VI 1037 emission lines. The Doppler dimming/pumping technique is based on the Doppler shift seen by the scattering particles, in the radiation from the lower layers of the solar atmosphere, which is caused by a net outflow of the scattering particles. As a result, the intensity of the scattered radiation will be reduced, compared to a situation with no outflow. This is called Doppler dimming. Eventually, the scattering particles might move so fast that they no longer experience resonance with "their" spectral emission line. If the outflow velocity of the scattering particles becomes large enough that they experience resonance with a neighboring emission

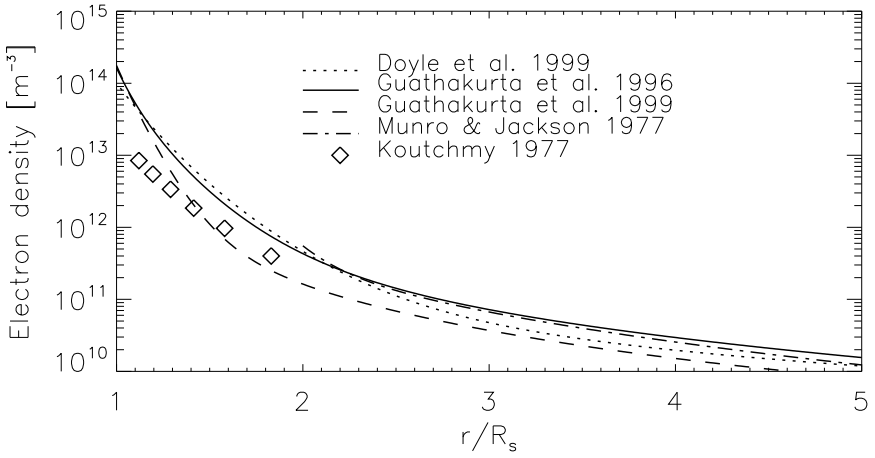

Figure 2.3: Observed electron density profiles in coronal holes, plotted vs. radial distance from the solar center.

line, from a different ion, the scattered radiation will be increased again. This is called Doppler pumping (*Kohl et al.*, 2006).

2.3 Acceleration of the fast solar wind

Hollweg (2006) describes three mechanisms for acceleration of the fast solar wind that have been much discussed. The first is that of *Parker* (1958), who introduced the electron pressure gradient as the driver of the solar wind. Parker showed that a hot corona, such as the solar corona, in static equilibrium, and dominated by thermal conduction, will have an asymptotic pressure that is several orders of magnitude greater than the pressure of the interstellar medium. The result is an expansion of the solar atmosphere into interplanetary space, i.e. a solar wind. The ultimate energy source for the solar wind, in the treatment of *Parker* (1958), is the physical processes responsible for heating the corona. In the following, we calculate the asymptotic pressure of a static corona, the treatment follows that of *Parker* (1958).

We assume a spherically symmetric hydrogen corona in static equilibrium with a radial magnetic field. We further assume quasi-neutrality and that the gas in the corona is fully ionized, giving a total kinetic pressure of $2NkT$, where N is the density, k is Boltzmann's constant and T is the temperature. With these assumptions, the equation of motion reduces to

$$0 = \frac{d}{dr}(2NkT) + \frac{GM_{\odot}MN}{r^2}, \tag{2.1}$$

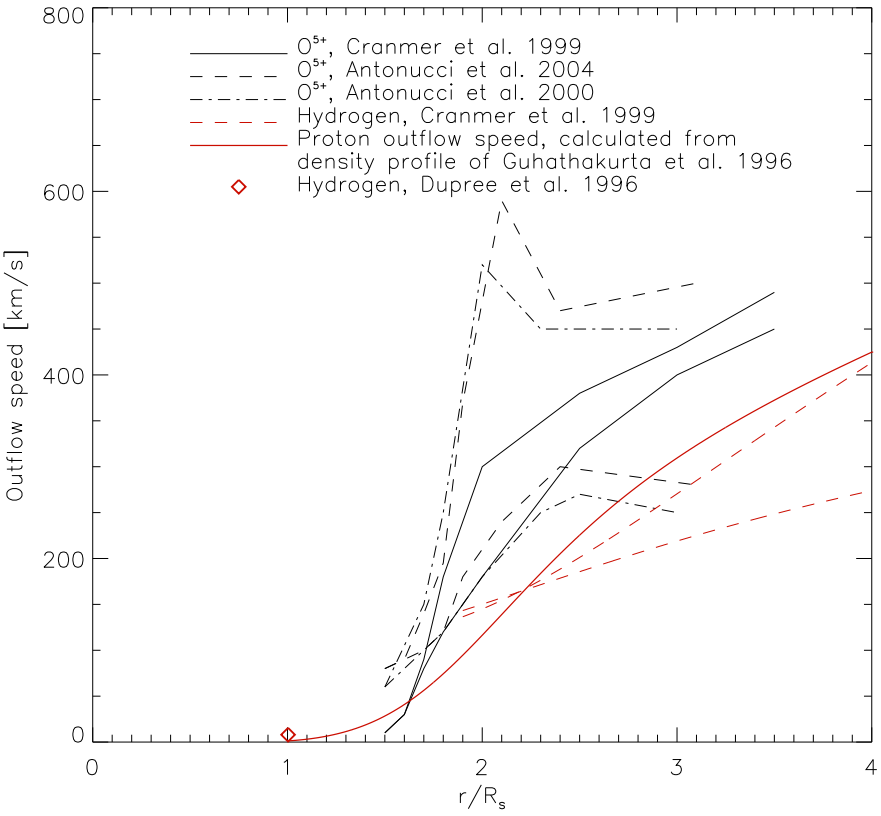

Figure 2.4: O^{5+} and hydrogen outflow velocities in coronal holes, and proton outflow velocity estimated by using mass conservation and the density profile of *Guhathakurta et al.* (1996), plotted vs. radial distance from the solar center.

where G is Newtons gravitational constant, M is the proton mass, $M_\odot$ is the solar mass and r is the distance from the center of the sun. At large distances from the sun, where there are no local heat sources, the steady state energy balance equation is

$$\nabla \cdot [\kappa(T)\nabla T] = \frac{1}{r^2}\frac{\partial}{\partial r}\left(r^2\kappa(T)\frac{\partial T}{\partial r}\right) = 0. \tag{2.2}$$

For collision dominated, fully ionized hydrogen of coronal densities, the thermal conductivity is (*Chapman*, 1954)

$$\kappa(T) = \kappa_0 T^n, \tag{2.3}$$

giving,

$$r^2\kappa_0 T^n \frac{\partial T}{\partial r} = C, \tag{2.4}$$

where $n = 2.5$.
By integration of equation 2.4,

$$\int_{r_0}^{r} \frac{C}{\kappa_0}\frac{1}{r^2}\partial r = \int_{T_0}^{T} T^n \partial T, \tag{2.5}$$

we obtain

$$T(r) = \left[\frac{A}{r} + B\right]^{\frac{1}{n+1}}, \tag{2.6}$$

where

$$A = \frac{-C(n+1)}{\kappa_0}, \tag{2.7}$$

and,

$$B = {T_0}^{n+1} + \frac{C(n+1)}{\kappa_0 r_0}. \tag{2.8}$$

Assuming that $T(\infty) = 0$ and $T(r_0) = T_0$ we have

$$T(r) = T_0\left[\frac{r_0}{r}\right]^{\frac{1}{n+1}}. \tag{2.9}$$

From equation 2.1 we get

$$d(2NkT) = 2kTdN + 2NkdT = -\frac{GM_\odot MN}{r^2}dr, \tag{2.10}$$

and, by inserting equation 2.9 into equation 2.10, and dividing by $2NkT$, we obtain

$$\frac{1}{N}dN = -\frac{1}{T}dT - \lambda r_0^{\frac{n}{n+1}} r^{\frac{-2n-1}{n+1}} dr, \tag{2.11}$$

where

$$\lambda = \frac{GM_\odot M}{2kT_0 r_0}. \tag{2.12}$$

By integration of equation 2.11,

$$\int_{N_0}^{N} \frac{1}{N}dN = -\int_{T_0}^{T} \frac{1}{T}dT - \lambda r_0^{\frac{n}{n+1}} \int_{r_0}^{r} r^{\frac{-2n-1}{n+1}} dr, \tag{2.13}$$

we find an expression for $N(r)$,

$$\ln\left(\frac{N(r)}{N_0}\right) = -\ln\left(\frac{T(r)}{T_0}\right) + \frac{\lambda(n+1)}{n}\left[\left(\frac{r_0}{r}\right)^{\frac{n}{n+1}} - 1\right], \tag{2.14}$$

or, by using the expression for $T(r)$ in equation 2.9,

$$N(r) = N_0\left(\frac{r}{r_0}\right)^{\frac{1}{n+1}} \exp\left(\frac{\lambda(n+1)}{n}\left[\left(\frac{r_0}{r}\right)^{\frac{n}{n+1}} - 1\right]\right). \tag{2.15}$$

Again using the expression for $T(r)$ in equation 2.9, we find an expression for the pressure, $p(r) = 2NkT$,

$$p(r) = p_0 \exp\left(\frac{\lambda(n+1)}{n}\left[\left(\frac{r_0}{r}\right)^{\frac{n}{n+1}} - 1\right]\right), \tag{2.16}$$

where $p_0 = 2N_0kT_0$. As $r \to \infty$, the pressure,

$$p \to p_0 \exp\left(\frac{-\lambda(n+1)}{n}\right). \tag{2.17}$$

Parker argued that for the corona to be in static equilibrium, this pressure must be balanced by the pressure of the interstellar medium. For typical values of the density and temperature of the corona and the interstellar medium, Parker found that this could not be done. If we take $N_0 = 10^{12}m^{-3}$, $T_0 = 10^6$ K and $r_0 = 2R_\odot$ we find that the asymptotic pressure is $8.5 \cdot 10^{-9}N/m^2$. The interstellar pressure is of order $10^{-19}N/m^2$ ($N_{IS} \approx 10^4 m^{-3}, T_{IS} \approx 3K$ (*Nordling and Österman*, 2004, Physics Handbook)). Parker concluded that since the pressure of the interstellar medium cannot balance the asymptotic pressure of a static solar atmosphere, the solar atmosphere must expand, forming a solar wind.

A solar wind was indeed observed (*Neugebauer and Snyder*, 1966), however the flow speed and the temperatures observed in the solar wind did not

match those predicted by the theoretical models of the time (*Parker*, 1965; *Hartle and Sturrock*, 1968). The predicted velocities and temperatures were too low compared with the observed values. Both *Parker* (1965) and *Hartle and Sturrock* (1968) concluded that heating of some sort must occur in the interplanetary medium.

In the early seventies the presence of Alfvén waves in the solar wind was discovered (*Belcher and Davis Jr.*, 1971), and it was proposed that the wave-pressure exerted by Alfvén waves on the wind might be responsible for accelerating the wind to the high velocities observed. The magnetic field force term in the equation of momentum in the Magnetohydrodynamic (MHD) approximation is

$$\mathbf{j} \times \mathbf{B} = \frac{1}{\mu_0}(\nabla \times \mathbf{B}) \times \mathbf{B}. \tag{2.18}$$

Since the interplanetary medium is very variable, it is convenient to use a time-average of the magnetic field force term. By using the vector relation

$$(\nabla \times \mathbf{A}) \times \mathbf{A} = (\mathbf{A} \cdot \nabla)\mathbf{A} - \mathbf{A}(\nabla \cdot \mathbf{A}), \tag{2.19}$$

and by noting that

$$\nabla \cdot \mathbf{B} = 0, \tag{2.20}$$

we find that

$$\left\langle \frac{1}{\mu_0}(\nabla \times \mathbf{B}) \times \mathbf{B} \right\rangle = \left\langle \frac{1}{\mu_0}(\mathbf{B} \cdot \nabla)\mathbf{B} \right\rangle, \tag{2.21}$$

where the angle-brackets denote a time-average. Using the relation

$$\nabla(\mathbf{B} \cdot \mathbf{B}) = \nabla(B^2) = (\mathbf{B} \cdot \nabla)\mathbf{B} + (\mathbf{B} \cdot \nabla)\mathbf{B} = 2(\mathbf{B} \cdot \nabla)\mathbf{B}, \tag{2.22}$$

we obtain

$$\left\langle \frac{1}{\mu_0}(\nabla \times \mathbf{B}) \times \mathbf{B} \right\rangle = \frac{1}{2\mu_0} \left\langle \nabla B^2 \right\rangle. \tag{2.23}$$

For Alfvén waves we know that

$$\mathbf{B} = \mathbf{B_0} + \partial\mathbf{B}, \tag{2.24}$$

where

$$\partial\mathbf{B} \perp \mathbf{B_0}. \tag{2.25}$$

This gives us the result

$$\left\langle \frac{1}{\mu_0}(\nabla \times \mathbf{B}) \times \mathbf{B} \right\rangle = \frac{1}{2\mu_0}\nabla \left\langle \partial \mathbf{B}^2 \right\rangle + \frac{1}{2\mu_0}\nabla \left\langle {\mathbf{B_0}}^2 \right\rangle . \qquad (2.26)$$

The first term on the right hand side in equation 2.26 can be thought of as the gradient of the magnetic field pressure caused by the magnetic field perturbations of the Alfvén waves. If we consider the magnetic field forces acting on the solar wind plasma, the second term on the right hand side in equation 2.26 is zero, because the background field is not associated with any local currents. Early modeling showed that the Alfvén-wave pressure gradient force was able to account for the solar wind velocities observed at 1 AU (*Belcher*, 1971; *Alazraki and Couturier*, 1971). *Hollweg* (1973) showed that damping of the Alfvén waves could heat the protons to temperatures in agreement with the observed values at 1 AU.

One important observational constraint on solar wind models is the electron density in the region close to the sun. Measurements have shown that the electron density declines very rapidly with increasing distance from the sun (e.g. *Guhathakurta et al.*, 1996, 1999). From the equation of continuity we know that, given a steady state condition, the mass flux (nu) of the solar wind is conserved. Thus, a rapidly declining density implies a rapidly increasing outflow velocity. The models based on acceleration by the wave-pressure gradient force were not able to explain this feature, because the wave-pressure term in the momentum equation is small compared to other terms close to the sun. The change in kinetic energy caused by the Alfvén wave pressure gradient, $\frac{\partial}{\partial t}(\frac{1}{2}u^2)_{Aw} = \mathbf{u} \cdot \nabla \mathbf{P}_{Aw}$ (subscript Aw meaning Alfvén wave) is small when $\mathbf{u}$ and $\mathbf{P}_{Aw}$ are both small. In the region close to the sun, both the flow speed and the amplitude of the magnetic field fluctuations of the Alfvén waves are expected to be small (*Hollweg*, 1978).

Anisotropies in the velocity distribution functions of the minor ions and protons (with $T_\perp \geq T_\parallel$) have been deduced from observations made with the Ultraviolet Coronagraph Spectrometer (UVCS) on the Solar and Heliospheric Observatory (SOHO) (e.g. *Frazin et al.*, 2003; *Kohl et al.*, 1998; *Cranmer et al.*, 1999).

The anisotropies in the velocity distribution functions indicate that heating by waves through the ion cyclotron resonance might be responsible for the rapid acceleration close to the sun. Ion cyclotron resonance occurs when a gyrating ion encounters an electromagnetic wave oscillating at the ion cyclotron frequency, i.e. when $|\omega - u_{\parallel i}k_\parallel| = \Omega_i$, where ω is the angular frequency of the electromagnetic wave, $k_\parallel$ is the wavenumber of the electromagnetic wave along the magnetic field, $u_{\parallel i}$ is the velocity of the ion parallel to the magnetic field and Ω_i is the ion cyclotron frequency. It is believed that Alfvén waves can heat the protons through the ion cyclotron resonance, thus creating a large proton pressure gradient force which can accelerate the particles.

In a static, spherically symmetric corona with isotropic pressure, no

heating above e.g. $2R_\odot$ and negligible heat conduction, the energy equation in the region above $2R_\odot$ can be written

$$(r^2\rho u)(\frac{1}{2}u^2 + \frac{\gamma}{\gamma-1}\frac{p}{\rho} + \phi) = const, \tag{2.27}$$

where γ is the ratio of specific heats $\frac{C_p}{C_v}$, p is the pressure, ρ is the mass density, u is the flow speed, r is the radial distance from the center of the sun and ϕ is the gravitational potential. If we also assume that $T_e = 0$, so that the solar wind is driven entirely by the proton pressure gradient, we can write

$$\frac{1}{2}{u_E}^2 + \frac{\gamma}{\gamma-1}\frac{kT_{pE}}{m} + \frac{GM_\odot}{r_E} = \frac{1}{2}{u_C}^2 + \frac{\gamma}{\gamma-1}\frac{kT_{pC}}{m} + \frac{GM_\odot}{r_C}, \tag{2.28}$$

where $m = (m_e + m_p)/2 \approx m_p/2$, G is the gravitational constant, k is the Boltzmann constant, T_p is the proton temperature, $M_\odot$ is the solar mass and the subscript E means the value at earth orbit while the subscript C denotes the value in the corona. Taking u_C equal to 1 km/s, u_E equal to 800 km/s and T_{pE} equal to $2.3{\cdot}10^5$ K (average proton temperature in the fast solar wind at at 1 AU from *Schwenn* (1990)), we find that $\frac{1}{2}{u_C}^2/\frac{1}{2}{u_E}^2$ and $\frac{kT_{pE}}{m}/\frac{1}{2}{u_E}^2$ are less than 10^{-2}, meaning that these terms can be neglected. If we further assume that $\gamma = 5/3$, we find that the proton temperature in the corona is $9 \cdot 10^6$ K. According to observations, proton temperatures in coronal holes range from $2 - 4 \ \cdot 10^6$ K (*Esser et al.*, 1999; *Kohl et al.*, 1997; *Cranmer et al.*, 1999). This simple calculation indicates that the proton pressure gradient plays an important role in the acceleration of the fast solar wind. However, in order to obtain the high velocities observed in the fast solar wind, heating must also occur above $2R_\odot$. Acceleration of the solar wind through the wave pressure gradient force, and the proton pressure gradient force, relies on energy addition to the solar wind through Alfvén waves. The waves are probably produced by the convective motions of the photospheric and convective zone plasma. They can be excited directly, i.e. magnetic field disturbances produced by the motion of the field line footprints in the photosphere, or through magnetic reconnection caused by magnetic field shears.

In the end, the question of how the solar wind is accelerated, and in particular, the relative importance of the different physical mechanisms involved in the different regions of the heliosphere has not yet been fully resolved.

2.4 Coronal source region of the fast solar wind

2.4.1 Supergranular cells and the chromospheric network

In the convection zone, hot plasma rises to the surface, where it cools, and then sinks back down into the solar interior. We can see the top of the small-scale convection cells on the solar surface, and we call them granules. The typical scale of a granule is 1000 km. There are also large-scale convective cells, called supergranules, with typical scales of 30 000 km.

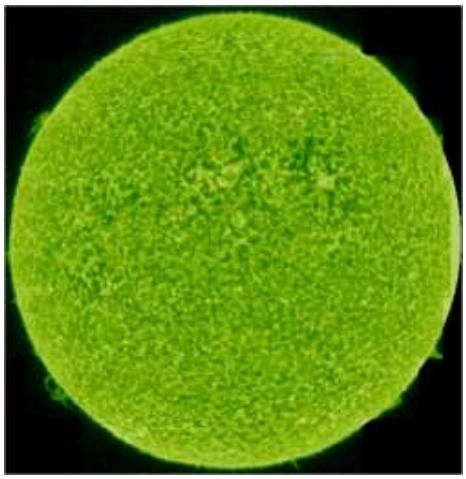

Figure 2.5: Image of the sun showing the chromospheric network, taken in the C III emission line at 977.020 Å, by the Solar Ultraviolet Measurements of Emitted Radiation (SUMER) instrument on-board the SOHO spacecraft. Courtesy of SOHO/SUMER consortium. SOHO is a project of international cooperation between ESA and NASA.

The borders of the supergranular cells are spatially correlated with the chromospheric network, which can be seen in figure 2.5 as a bright patchy web on the solar surface. Owing to the extremely high conductivity of the convection zone-plasma, the magnetic field is frozen into it. When the plasma travels trough the convection zone to the solar surface, it brings the magnetic field with it. The flow of plasma on the solar surface, from the middle of the supergranules, towards the edge, transports magnetic field lines towards the edges of the cells, where one can observe strong magnetic fields. The chromospheric network was found to be spatially correlated with the magnetic field enhancements found at the supergranular cell borders (*Leighton et al.*, 1962; *Noyes and Leighton*, 1963; *Simon and Leighton*, 1964).

Gabriel (1976) proposed a magnetic field model of the coronal holes where a "channel", or flow tube, of open field lines emerge from the chromospheric network and expand above the supergranular cells. *Gabriel* (1976) also suggested that the fast solar wind has its origin in such channels. Figure 2.6 (from *Holzer* (2005)) is a schematic illustration of the upper part of the convection zone, and the solar atmosphere, showing the flow pattern of the supergranular cells, and the magnetic field structures associated with granular, and supergranular convection. The location of the magnetic field structures associated with the chromospheric network is also indicated (labeled "Network"). The boundaries of the polar coronal holes do not extend

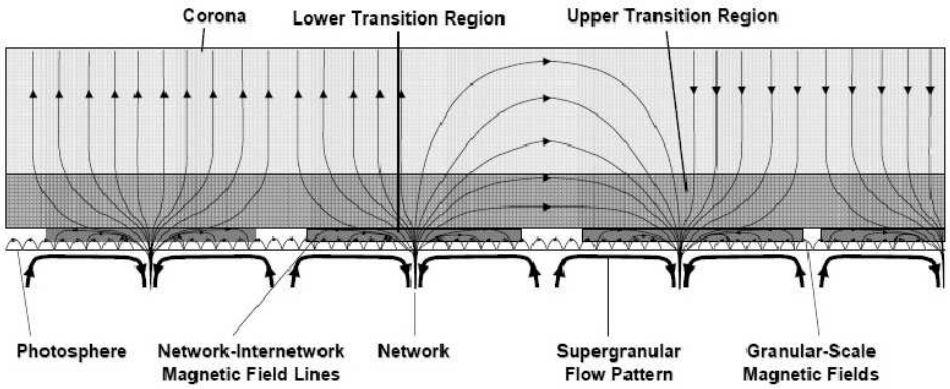

Figure 2.6: Schematic illustration of the upper convection zone and solar atmosphere showing the flow pattern of the supergranular cells (thick solid lines) and the magnetic field structures (thin solid lines) associated with granular (small loops) and supergranular convection. The light gray area is the corona, the dark gray area is the upper transition region and the dark gray and white area is the lower transition region. Also indicated is the location of the magnetic field structures associated with the chromospheric network. The illustration is adopted from *Holzer* (2005).

below 50° latitude at solar minimum (e.g. *Harvey*, 1996), however fast solar wind streams have been observed as low as 30° latitude by the Ulysses spacecraft (e.g. *Gosling et al.*, 1995). To explain this, it has been proposed that the flow tubes may expand super-radially, (e.g. *Munro and Jackson*, 1977; *Zirker*, 1977) as shown in figure 2.6, where the magnetic field emerging from the supergranular cell borders expand super-radially in a small region close to the sun (in the chromosphere and lower transition region). The degree of expansion of the magnetic flow tubes is a question yet to be answered.

2.4.2 Plumes

When observing a coronal hole in Extreme Ultraviolet (EUV) light, it appears as a large dark spot on the solar surface. This is because the plasma inside a coronal hole is cooler, and less dense than in the surrounding regions. However, within the coronal hole there are also brighter regions. In polar coronal holes these bright features can be seen as long ray-like structures extending out from the solar surface. They are called plumes, and the darker regions surrounding them are called inter-plume regions, or inter-plume lanes. Figure 2.7 shows a polar coronal hole (dark region) with plumes, captured in the Fe XII emission line by the SOHO - Extreme ultraviolet Imaging Telescope (EIT).

Plumes are open magnetic field structures that are rooted in the chro-

Figure 2.7: Image of the sun showing a coronal hole (dark region) and plumes (bright spots/rays inside the coronal hole), in the Fe XII emission line taken by EIT on-board the SOHO spacecraft. Courtesy of SOHO/EIT consortium. SOHO is a project of international cooperation between ESA and NASA.

mospheric network, in regions of concentrated, unipolar magnetic flux (e.g. *Harvey*, 1965; *Newkirk and Harvey*, 1968; *Deforest et al.*, 1997; *Hassler et al.*, 1997). Although coronal holes are dominated by open magnetic field lines, mixed polarity structures are also present, and at larger distances from the solar surface, the plumes seem to trace the open-field regions of the coronal hole (*Deforest et al.*, 1997).

Wang et al. (1997) and *Wang and Sheeley* (1995) found that polar plumes occur near the boundary between mixed polarity fields and unipolar field concentrations. However, not all mixed polarity structures inside coronal holes give rise to a polar plume. *Wang and Sheeley* (1995) proposed that plumes are created as a result of magnetic reconnection between bipolar fields (loops) inside the coronal hole and nearby unipolar fields (open field configurations).

The degree of expansion of the magnetic field embedded in the plumes is not established. *Fisher and Guhathakurta* (1995); *Deforest et al.* (1997) and *DeForest et al.* (2001) have found evidence of super-radial expansion of the plumes. However, *Woo and Habbal* (1999) and *Woo et al.* (1999) reports observations suggesting radial expansion of the plumes.

Several authors have measured temperatures and densities (*Cranmer et al.*, 2001; *Del Zanna et al.*, 2003; *Del Zanna*, 2003; *Wilhelm*, 2006) and outflow velocities (*Antonucci et al.*, 1997; *Giordano et al.*, 2000; *Gabriel et al.*, 2003; *Wilhelm et al.*, 1998; *Gabriel et al.*, 2004, 2005) in plumes. There seems to be a general agreement that plumes are denser and cooler

than the inter-plume regions.

In the case of the outflow velocities, which are particularly important for determining the source regions of the fast solar wind, observational results are more confusing. *Gabriel et al.* (2003) found that in the height region between 1.05 and $1.35R_{\odot}$ the outflow velocity in plumes is greater than in the inter-plume region. This is consistent with observations by *Gabriel et al.* (2004). *Gabriel et al.* (2005) found that outflow velocities in plumes are larger than outflow velocities in the inter-plume regions close to the sun (below $1.6R_{\odot}$), while the opposite is true above this height. On the other hand, *Antonucci et al.* (1997) found that the outflow velocity in plumes is lower than in the inter-plume region in the height region 1.45 to $2.34R_{\odot}$. This is consistent with the observations of *Giordano et al.* (2000). *Hassler et al.* (1999) measured the blue-shift of Ne^{7+} in a polar coronal hole. They found that the line-of-sight velocity (see chapter 3) was no greater inside the two plumes that were observed in this coronal hole, than outside them. The results of *Gabriel et al.* (2003, 2005) are also in disagreement with theoretical studies of outflow in polar plumes (*Raouafi et al.*, 2007; *Wang*, 1994). *Raouafi et al.* (2007) compares observed spectral line profiles of hydrogen and O^{+5} in coronal holes to synthesized spectral line profiles calculated with a theoretical model. They have assumed that the spectral profiles are produced by a plasma population consisting of one narrow Maxwellian particle velocity distribution, corresponding to the plume plasma, and one broad distribution, corresponding to the inter-plume plasma. They argue that a higher velocity in the plumes, should be reflected in a Doppler shift of the spectral profile corresponding to the narrow distribution, relative to the spectral profile corresponding to the broad distribution. Such a shift is not found in the observed spectral line profiles.

The observations of outflow velocities discussed above are all spectroscopic observations based on ionic emission lines and most of them measure the outflow velocities of minor ions, mainly oxygen. Whether the outflow velocities deduced from observations of minor ion emission lines reflect the outflow velocity of the background proton-electron solar wind in this height region is not known.

The question of whether it is the plumes or the inter-plume regions that are the main source regions of the fast solar wind has not yet been answered, but as mentioned earlier, it is agreed that the fast solar wind originates from the regions of concentrated magnetic flux that outlines the supergranular cells, where the plumes are also rooted.

Chapter 3

Observations of minor ion outflow

The line-of-sight velocities (i.e., the velocity in the direction of the line of sight of the observer) of minor ions in the solar atmosphere, can be determined by evaluating the Doppler shift of the radiation emitted by the ions. For observed radiation at a wavelength λ, from ions emitting at a wavelength λ_0 (determined theoretically or in a laboratory), the component along the line-of-sight of the bulk velocity of the ions, u_{LOS}, is given by

$$u_{LOS} = \frac{(\lambda - \lambda_0)c}{\lambda_0}, \tag{3.1}$$

(*Kohl et al.*, 2006).

Spectral lines from emitting ions are broadened by various physical mechanisms, and usually have a spectral line profile (intensity vs. wavelength) that resembles a Maxwellian. To determine the bulk velocity along the line of sight, λ is usually taken to be the wavelength of maximum intensity.

Emission lines that are shifted towards shorter wavelengths are said to be blue-shifted, while emission lines that are shifted towards longer wavelengths are said to be red-shifted. A blue-shift in the emission line of an ion, means that the ion has a bulk velocity towards the observer, and away from the solar surface, while a red-shift means that the ions emitting the radiation are traveling down towards the surface of the sun. The flow velocities can be estimated from measured blue-shifts by making some assumptions about the flow geometry, i.e. on whether the component of the bulk velocity of the ions, along the line of sight of the observer, is large or small compared to the total flow velocity. It is important to keep in mind that, because of the uncertainty introduced through assumptions on flow geometry, the errors in the estimated flow velocities may be significant. These errors also have to be added to the observational uncertainty in the measurements of the blue-shifts, which typically ranges from 1-3 km/s (*Xia et al.*, 2003; *Tu*

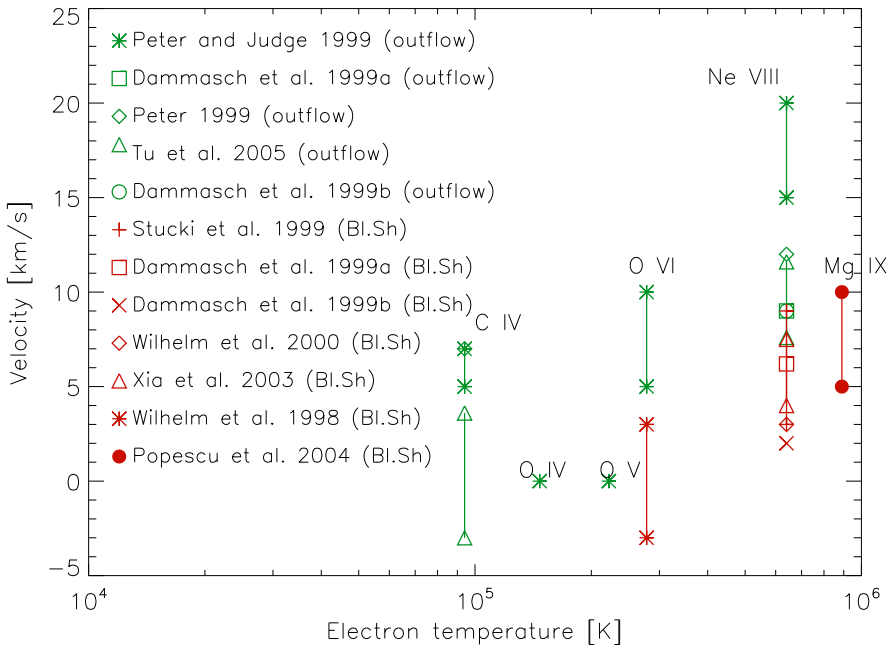

Figure 3.1: Measured blue-shifts (Bl.Sh) and estimated outflow velocities (outflow) for the six ions listed in table 3.1, plotted vs. formation temperature.

et al., 2005; *Peter and Judge*, 1999).

Figure 3.1 shows estimated flow velocities and measured blue-shifts plotted vs. formation temperature for six different ions of carbon, oxygen, neon and magnesium. By the formation temperature of an ion, we mean the electron temperature in the region of the solar atmosphere where the ion fraction is at its maximum value. The ion fraction, x_i, of the charge state i (e.g. i=5 for O^{5+}) of an element is defined as $x_i = n_i/n_{el}$.

For all the ions where multiple observations are available, we find that the range of flow velocities and blue-shifts found by different authors is large. The Ne VIII line is by far the best documented, and it also has the largest range of observed flow velocities. The Ne VIII line is on average blue-shifted inside coronal holes, (*Xia et al.*, 2004, 2003) and exhibits a clear blue-shift in all the observations in figure 3.1. Observations of the Ne VIII line also show that the blue-shift is larger in areas of strong outwardly directed magnetic flux (e.g. *Xia et al.*, 2004; *Hassler et al.*, 1999; *Xia et al.*, 2003).

Both the C IV line and the O VI line have been found to be both red-shifted and blue-shifted by different authors. *Xia et al.* (2004) found that the O VI line was on average red-shifted, but that it could also be blue-shifted in regions of strong, outwardly directed magnetic flux. *Xia et al.* (2004)

found that emission lines coming from ions that are formed in the transition region are on average red-shifted in coronal holes. A similar result was obtained by *Popescu et al.* (2004), who measured the Doppler-shift of the O III line. They found that the O III line was on average red-shifted in the coronal hole, but that blue-shifts also occurred, mainly on the chromospheric network boundaries.

These results are consistent with the idea that fast solar wind originates in the regions of concentrated magnetic flux that outlines the supergranular cells. It is reasonable to expect that the largest outflows of minor ions, as well as protons will be found in the source regions of the solar wind.

The ions are also listed in table 3.1, together with their formation temperature and the wavelength of the emission line. The formation temperatures in figure 3.1 have been calculated by solving for the equation of continuity in the numerical model of *Hansteen and Leer* (1995); *Lie-Svendsen et al.* (2001, see equation 4.6 in section 4.1), with $u_s = 0$ and the left hand side equal to zero (i.e. assuming ionization equilibrium), and using atomic data from the High Altitude Observatory Spectral Diagnostic Package for Emitted Radiation (HAOS-DIAPER) (*Judge and Meisner*, 1994). We have also calculated the formation temperatures of these six ions using ionization and recombination rates from *Mazzotta et al.* (1998).

Ion	$T_f[10^5K](1)$	$T_f[10^5K](2)$	$T_f[10^5K](3)$	λ_0[Å]
C^{3+}(C IV)	0.94	1	1	1548
O^{3+}(O IV)	1.47	1.58	1.87	1401
O^{4+}(O V)	2.22	2.51	2.4	630
O^{5+}(O VI)	2.78	3.16	2.8	1038
Ne^{7+}(Ne VIII)	6.4	6.31	6.49	770
Mg^{8+}(Mg IX)	8.9	10	N/A	706

Table 3.1: The ionization equilibrium formation temperatures and the wavelengths of the emission lines for the six ions investigated in this thesis, calculated using ionization and recombination rates from different atomic tables.(1): from HAOS-DIAPER (*Judge and Meisner*, 1994) (2): from *Mazzotta et al.* (1998) (3): from *Landini and Monsignori Fossi* (1990)(taken from *Peter and Judge* (1999). N/A: Not Available

The atomic data from HAOS-DIAPER (*Judge and Meisner*, 1994) give the lowest formation temperatures for all ions, except Ne^{7+}. The difference in formation temperature between different sets of atomic data is largest for O^{4+} and O^{5+}, where the formation temperature for the *Mazzotta et al.* (1998) atomic data is 13% higher than the formation temperature for the atomic data from *Judge and Meisner* (1994).

Chapter 4

The theoretical model

In this chapter we will introduce the equations used to calculate the densities, temperatures and outflow velocities for the background proton-electron solar wind as well as for the minor ions. We will also explain two of these equations in some detail, the equation of continuity, and the equation of motion. These equations are particularly important to understand when we analyze our results later on. Finally, we will present the two background models used in the calculations for the minor ions.

4.1 The model equations

The numerical model (*Hansteen and Leer*, 1995; *Lie-Svendsen et al.*, 2001) is based on the newly developed gyrotropic transport equations described in *Janse et al.* (2005). The equations have been calculated by multiplying the Boltzmann equation with moments of the velocity distribution function, and integrating over velocity space. It is possible to do this without specifying a velocity distribution function, but this will not yield a closed set of equations. The transport equation for the velocity moment of order k will include the velocity moment of order k+1. Thus, in order to obtain a closed set of equations we must make an assumption about the velocity moment of highest order in our equations (assume some relation to the lower order velocity moments), or we must assume a velocity distribution function, so that we can calculate the velocity moment of highest order in terms of the lower order velocity moments. *Janse et al.* (2005) have assumed a velocity distribution function that is believed to describe the plasma in the solar atmosphere, and the solar wind, well, and have developed transport equations for the density, momentum, pressure and heat flux. The term gyrotropic means that the assumed velocity distribution function allows for different temperatures in the direction parallel to, and perpendicular to (i.e., in the plane of gyration) the magnetic field. The velocity distribution function is also symmetric in the plane perpendicular to the magnetic field. This

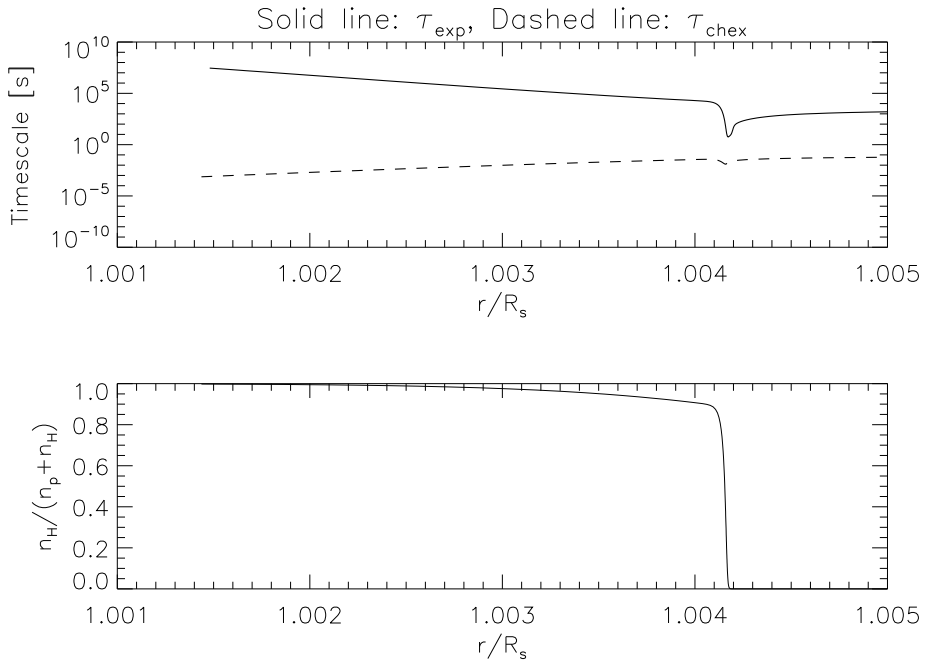

Figure 4.1: Expansion and charge exchange timescales (top panel) and ion fraction (bottom panel) for hydrogen, plotted vs. radial distance from the solar center.

symmetry in the velocity distribution function implies that the transport of particles, momentum and energy occurs strictly along the magnetic field. The model is one-dimensional, and it is assumed that the plasma flows in a flow tube, which is a magnetic flux tube, of infinitesimal cross section. The expansion of the flow tube, which is given by the expansion of the magnetic field, is radial, except in a very small region, where the expansion might be super-radial. However, since the cross section of the tube is infinitesimal, the flow is radial everywhere, and everywhere parallel to the magnetic field. The radial component of the divergence of a vector, $\mathbf{B}$, in spherical coordinates is

$$\nabla \cdot \mathbf{B} = \frac{1}{r^2}\frac{\partial}{\partial r}(r^2 B_r) = \frac{\partial B_r}{\partial r} + B_r \frac{2}{r}. \tag{4.1}$$

By using Gauss' theorem,

$$\int \nabla \cdot \mathbf{B} dV = \oint \mathbf{B} \cdot d\mathbf{S} \tag{4.2}$$

it can be shown that the divergence of a vector, $\mathbf{B} = B_r \hat{\mathbf{r}}$, (where $\hat{\mathbf{r}}$ is the unit vector in the radial direction)

$$\nabla \cdot \mathbf{B} = \frac{1}{A}\frac{\partial}{\partial r}(AB_r) = \frac{\partial B_r}{\partial r} + B_r\frac{1}{A}\frac{\partial A}{\partial r}, \tag{4.3}$$

where A is the cross sectional area of the flow tube. Thus, in the equations used in the numerical model, the factor $\frac{2}{r}$ is replaced by $\frac{1}{A}\frac{\partial A}{\partial r}$.

Since neutral hydrogen is not affected by the magnetic field, one might question the assumption that the transport of all particles, also neutral atoms, occurs strictly along the magnetic field throughout the entire height region in the model, as implied by the symmetry in the velocity distribution function in the plane perpendicular to the magnetic field. However, because of charge exchange with a small population of protons, the individual hydrogen atoms can feel the magnetic field in the short, but frequent, periods of time when they are stripped of their electron. When the timescale for charge exchange is much smaller than the timescale for expansion, the flow of hydrogen is affected by the magnetic field, and the assumption above is valid. The neutral minor species are coupled to the background solar wind in the region where they are dominant, and thus, the assumtion of radial transport is valid for them as well. The expansion timescale for hydrogen, is given by

$$\tau_{exp} = \left| \frac{n_H + n_p}{u_H} \left(\frac{\partial (n_H + n_p)}{\partial r} \right)^{-1} \right|, \tag{4.4}$$

and is the time it takes for the hydrogen particles to travel through one scale height of hydrogen-proton density.
The timescale for charge exchange between hydrogen and protons, is given by

$$\tau_{chex} = \frac{1}{(R_{Hp})_{chex}}. \tag{4.5}$$

If we concider a small volume of partially ionized hydrogen gas, $(R_{Hp})_{chex}$ is the fraction of the total hydrogen population, that are stripped of an electron, as a result of charge exchange with protons, each second. In the top panel of figure 4.1 we have plotted the timescale for charge exchange between hydrogen and protons together with the expansion timescale in the upper chromosphere, as a function of distance from the solar center, for one of the two models we have used for the background solar wind (i.e. the hydrogen-proton-electron fluid. For a description of the background models see section 4.4.1). The ion fraction for neutral hydrogen is shown in the bottom panel. Throughout the region where neutral hydrogen dominates, the timescale for expansion is more than five orders of magnitude larger than the timescale for charge exchange. The result for the second background model is the same.

When assuming radial flow, the equations of *Janse et al.* (2005) reduce to five transport equations for matter, n_s, momentum, $m_s u_s$, temperature (parallel and perpendicular to the field), $T_{s\parallel/\perp}$, and heat flow, q_s, for each particle species, s. The equations used in the numerical model include some higher order frictional terms, and terms used to mimic the two-stream plasma instability in the outer solar wind. These terms have not been included in the equations presented here, because they are negligible in the region of interest to us, i.e. the transition region and lower corona.
Equation 4.6 is the equation of continuity, which is a conservation equation for matter.

$$\frac{\partial n_s}{\partial t} = -\frac{\partial}{\partial r}(n_s u_s) - n_s u_s \frac{1}{A}\frac{\partial A}{\partial r} + \frac{\delta n_s}{\delta t} \tag{4.6}$$

It contains the number density, n_s, the flow velocity, u_s, the cross sectional area of the flow tube, A, and the term $\frac{\delta n_s}{\delta t}$, which is the collisional term for the equation of continuity. $\frac{\delta n_s}{\delta t}$ is given by equation 4.7,

$$\frac{\delta n_s}{\delta t} = \sum_t (n_t R_{ts} - n_s R_{st}), \tag{4.7}$$

where R_{st} is the transition rate from charge state s, to charge state t as a result of photo-ionization, collisional ionization, recombination and charge exchange. In our simulations we have used transitional rates from HAOS-DIAPER (*Judge and Meisner*, 1994).
Equation 4.8 is the equation of motion.

$$\begin{aligned}\frac{\partial u_s}{\partial t} + u_s\frac{\partial u_s}{\partial r} &= -\frac{k}{m_s}\frac{\partial T_{s\parallel}}{\partial r} - \frac{kT_{s\parallel}}{n_s m_s}\frac{\partial n_s}{\partial r} - \frac{1}{A}\frac{dA}{dr}\frac{k}{m_s}(T_{s\parallel} - T_{s\perp}) + \frac{e_s}{m_s}E \\ &\quad -\frac{GM_\odot}{r^2} + \frac{1}{n_s m_s}\frac{\delta M_s}{\delta t}\end{aligned} \tag{4.8}$$

In addition to the symbols already mentioned in connection with equation 4.6 it contains the parallel and perpendicular temperature, $T_{s\parallel}$ and $T_{s\perp}$, the mass and charge of a particle of species s, m_s and e_s, the Boltzmann constant, k, the electric field, E, the solar mass, $M_\odot$, the gravitational constant, G, and the term $\frac{\delta M_s}{\delta t}$ is the collisional term in the equation of motion which is given by equation 4.9,

$$\begin{aligned}\frac{\delta M_s}{\delta t} &= -\sum_t n_s m_s \nu_{st}(u_s - u_t) \\ &+ \sum_t \nu_{st}\frac{3}{5}\frac{\mu_{st}}{kT_{st}}\left[q_s\left(1 - \frac{5}{7}\frac{m_t}{m_s + m_t}\right) - q_t\frac{m_s n_s}{m_t n_t}\left(1 - \frac{5}{7}\frac{m_s}{m_s + m_t}\right)\right] \\ &+ m_s\sum_t (n_t u_t R_{ts} - n_s u_s R_{st}).\end{aligned} \tag{4.9}$$

The reduced mass is

$$\mu_{st} = \frac{m_s m_t}{m_s + m_t}, \tag{4.10}$$

and the reduced temperature, T_{st}, is defined as

$$T_{st} = \frac{T_s m_t + T_t m_s}{m_s + m_t}, \tag{4.11}$$

where $T_s = (T_{s\parallel} + 2T_{s\perp})/3$ is the average temperature.
The coulomb collisional frequency is

$$\nu_{st} = \frac{1}{3}\frac{n_t m_t}{m_s + m_t}\left(\frac{2\pi k T_{st}}{\mu_{st}}\right)^{-3/2}\frac{{e_s}^2 {e_t}^2}{{\epsilon_0}^2 {\mu_{st}}^2}\ln\lambda, \tag{4.12}$$

where ϵ_0 is the permittivity of vacuum and $\ln\lambda$ is the coulomb logarithm. The coulomb logarithm is a factor which accounts for the Debye screening of the particles' electric fields. Owing to Debye screening, particles can only interact (i.e. they can only collide) if the distance between them is less than one Debye length. In the case of an electron colliding with a multiply charged ion, they need to be closer than the Debye length of the electron, because the electron has the shorter Debye length of the two.

Consider an electron with speed v, passing an ion of charge Ze at a distance l, called the impact parameter. We can estimate the change in perpendicular velocity of the electron by assuming that this situation is equivalent to a situation where a perpendicular force, equal to the coulomb force, acts on the electron for a time $t = l/v$. We find that

$$m_e \Delta v_\perp \approx Ft = \frac{Ze^2}{4\pi\epsilon_0}\frac{1}{vl}. \tag{4.13}$$

The maximum change in perpendicular velocity is given by energy conservation and is equal to $m_e v$. The distance of closest approach is thereby found to equal

$$\frac{Ze^2}{4\pi\epsilon_0}\frac{1}{m_e v^2}. \tag{4.14}$$

The coulomb logarithm is the logarithm of the maximum impact parameter (i.e. the Debye length), in units of the distance of closest approach.

The expression above (4.14), for the distance of closest approach, is only a coarse approximation, and in a plasma consisting of electrons and ions with given velocity distribution functions, the calculation of the coulomb logarithm will be more complicated. The expression for the coulomb logarithm used in the numerical model of *Hansteen and Leer* (1995); *Lie-Svendsen et al.* (2001) is

$$\ln\lambda = 23 - \ln\left[\left(\frac{n_e}{n_0}\right)^{1/2}\left(\frac{T_e}{T_0}\right)^{-3/2}\right], \tag{4.15}$$

where $T_0 = 10^6$ K, and $n_0 = 1m^{-3}$. In the numerical model, ion-neutral and neutral-neutral collisions are also included.
Equation 4.16 and 4.17 are the energy conservation equations, describing the change with time of the parallel and perpendicular temperature, in a frame moving with the fluid.

$$\begin{aligned}\frac{\partial T_{s\|}}{\partial t} + u_s\frac{\partial T_{s\|}}{\partial r} &= -2T_{s\|}\frac{\partial u_s}{\partial r} - \frac{1}{n_s k}\frac{\partial q_{s\|}}{\partial r} - \frac{1}{A}\frac{dA}{dr}\frac{q_{s\|}}{n_s k} + \frac{2}{A}\frac{dA}{dr}\frac{q_{s\perp}}{n_s k} \\ &\quad + \frac{1}{n_s k}Q_{sm\|} + \frac{1}{n_s k}\frac{\delta E_{s\|}}{\delta t}\end{aligned} \tag{4.16}$$

$$\begin{aligned}\frac{\partial T_{s\perp}}{\partial t} + u_s\frac{\partial T_{s\perp}}{\partial r} &= -\frac{1}{A}\frac{dA}{dr}u_s T_{s\perp} - \frac{1}{n_s k}\frac{\partial q_{s\perp}}{\partial r} - \frac{2}{A}\frac{dA}{dr}\frac{q_{s\perp}}{n_s k} + \frac{1}{n_s k}Q_{sm\perp} \\ &\quad + \frac{1}{n_s k}\frac{\delta E_{s\perp}}{\delta t}\end{aligned} \tag{4.17}$$

In addition to the symbols mentioned above they contain the parallel and perpendicular heat flux , $q_{s\|}$ and $q_{s\perp}$, the symbols $Q_{sm\|}$ and $Q_{sm\perp}$ which describe heating, e.g. by Alfvén waves, and the terms $\frac{1}{n_s k}\frac{\delta E_{s\perp}}{\delta t}$ and $\frac{1}{n_s k}\frac{\delta E_{s\|}}{\delta t}$ are the collisional terms of the energy conservation equations, given by equations 4.19 and 4.18,

$$\begin{aligned}\frac{\delta E_{s\|}}{\delta t} &= -\sum_t 2\frac{m_s}{m_s+m_t}n_s\nu_{st}k\left\{T_{s\|} - T_{t\|} - \frac{2}{5}\left[\frac{m_t}{m_s}(T_{s\perp} - T_{s\|})\right.\right. \\ &\quad \left.\left. + T_{t\perp} - T_{t\|}\right]\right\} + \sum_t (n_t k T_{t\|} R_{ts} - n_s k T_{s\|} R_{st}),\end{aligned} \tag{4.18}$$

$$\begin{aligned}\frac{\delta E_{s\perp}}{\delta t} &= -\sum_t 2\frac{m_s}{m_s+m_t}n_s\nu_{st}k\left\{T_{s\perp} - T_{t\perp} - \frac{1}{5}\left[\frac{m_t}{m_s}(T_{s\perp} - T_{s\|})\right.\right. \\ &\quad \left.\left. + T_{t\perp} - T_{t\|}\right]\right\} + \sum_t (n_t k T_{t\perp} R_{ts} - n_s k T_{s\perp} R_{st}).\end{aligned} \tag{4.19}$$

Equation 4.20,

$$\begin{aligned}\frac{\partial q_s}{\partial t} + u_s\frac{\partial q_s}{\partial r} &= -2q_{s\|}\frac{\partial u_s}{\partial r} - \frac{1}{2}u_s q_{s\|}\frac{1}{A}\frac{dA}{dr} - 2q_{s\perp}\frac{\partial u_s}{\partial r} - 2u_s q_{s\perp}\frac{1}{A}\frac{dA}{dr} \\ &\quad - \frac{k^2 n_s T_{s\|}}{m_s}\frac{\partial}{\partial r}\left(\frac{3}{2}T_{s\|} + T_{s\perp}\right) - \frac{1}{A}\frac{dA}{dr}\frac{k^2 n_s T_{s\perp}}{m_s}(T_{s\|} - T_{s\perp}) \\ &\quad + \frac{\delta {q_s}'}{\delta t},\end{aligned} \tag{4.20}$$

is the heat flow equation, where

$$\frac{\delta {q_s}'}{\delta t} = \frac{\delta q_s}{\delta t} - \frac{k}{m_s}\left(\frac{3}{2}T_{s\parallel} + T_{s\perp}\right)\frac{\delta M_s}{\delta t}, \tag{4.21}$$

has been introduced to simplify the equations, and $\frac{\delta q_s}{\delta t}$ is defined in equation 4.24. q_s is related to the parallel and perpendicular heat flow through the equations

$$q_{s\parallel} = 30q_s\frac{{T_{s\parallel}}^3(4T_{s\perp} + 3T_{s\parallel})}{16{T_{s\perp}}^4 + 48{T_{s\perp}}^3T_{s\parallel} + 6{T_{s\perp}}^2{T_{s\parallel}}^2 + 60T_{s\perp}{T_{s\parallel}}^3 + 45{T_{s\parallel}}^4}, \tag{4.22}$$

and

$$q_{s\perp} = 2q_s\frac{{T_{s\perp}}^2(8{T_{s\perp}}^2 + 24T_{s\perp}T_{s\parallel} + 3{T_{s\parallel}}^2)}{16{T_{s\perp}}^4 + 48{T_{s\perp}}^3T_{s\parallel} + 6{T_{s\perp}}^2{T_{s\parallel}}^2 + 60T_{s\perp}{T_{s\parallel}}^3 + 45{T_{s\parallel}}^4}. \tag{4.23}$$

As mentioned earlier, the transport of energy occurs strictly parallel to the magnetic field. The perpendicular heat flow, is a flow of perpendicular thermal energy, parallel to the magnetic field.
Equation 4.24,

$$\begin{aligned}\frac{\delta {q_s}'}{\delta t} &= -\sum_{t\neq s}\nu_{st}\left\{{E_{st}}^{(1)}q_s - {E_{st}}^{(4)}\frac{m_sn_s}{m_tn_t}q_t + \frac{5}{2}p_s(u_s - u_t)\right. \\ &\left.\left[1 - \frac{3}{5}\frac{m_t}{m_s + m_t}\right]\right\} - \frac{16}{35}\nu_{ss}q_s + \sum_t(q_tR_{ts} - q_sR_{st}),\end{aligned} \tag{4.24}$$

is the collisional term in the heat flow equation (4.20), where the mass factors ${E_{st}}^{(1)}$ and ${E_{st}}^{(4)}$ are defined as

$${E_{st}}^{(1)} \equiv \frac{1}{{m_0}^3}\left(3{m_s}^3 - \frac{1}{2}{m_s}^2m_t - \frac{2}{5}m_s{m_t}^2 - \frac{4}{35}{m_t}^3\right) \tag{4.25}$$

$${E_{st}}^{(4)} \equiv \frac{1}{{m_0}^3}\left(\frac{6}{5}{m_t}^3 - \frac{171}{70}{m_t}^2m_s - \frac{3}{7}m_t{m_s}^2\right). \tag{4.26}$$

The cross sectional area of the flow tube is given by (*Kopp and Holzer*, 1976):

$$A(r) = A_0\left(\frac{r}{R_\odot}\right)^2 f_1(r)f_2(r), \tag{4.27}$$

where, A_0 =1 m^2, is the area of the flow tube at the solar surface, and

$$f_i(r) = \frac{f_{max\,i} \exp\left[\frac{r-R_{1i}}{\sigma_i}\right] + f_{1i}}{\exp\left[\frac{r-R_{1i}}{\sigma_i}\right] + 1}, \tag{4.28}$$

where

$$f_{1i} = 1 - (f_{max\,i} - 1) \exp\left[\frac{R\odot - R_{1i}}{\sigma_i}\right]. \tag{4.29}$$

$f_i(r)$ is the expansion function and describes the expansion of the flow tube as a function of radial distance. As mentioned earlier, the flow tube expands radially throughout most of the region between the lower and upper boundary of the numerical model. The expression for the cross sectional area of the flow tube in 4.27, allows for non-radial expansion in two different regions along the flow tube. The first is the region surrounding R_{11}, and the second is the region surrounding R_{12}. At $R_{11}(R_{12})$, the cross sectional area of the flow tube increases to $f_{max1}(f_{max1}f_{max2})$ times the area of a radially expanding flow tube, and most of the increase occurs in the region $R_{11} - \sigma_1$ to $R_{11} + \sigma_1(R_{12} - \sigma_2$ to $R_{12} + \sigma_2)$. The maximum value of $\frac{\partial f_i}{\partial r}$ occurs at R_{1i}.

4.2 The equation of continuity

The equation of continuity for the particle species s, is

$$\frac{\partial n_s}{\partial t} + \nabla \cdot (n_s \mathbf{u_s}) = \frac{\delta n_s}{\delta t}. \tag{4.30}$$

Janse et al. (2005) derived equations for fully ionized gases, i.e. with the collisional term equal to zero. The model described in the previous section must also be able to describe the ionization of the neutral chromospheric gas, which occurs mainly in the transition region. For this reason, the collisional term in the numerical model must include loss and gain of particles by ionization and recombination. In the numerical model, the collisional term is equal to (equation 4.9) $\sum_t (n_t R_{ts} - n_s R_{st})$, where R_{st} is the rate of transitions from charge state s, to charge state t, as a result of photo-ionization, collisional ionization, recombination and charge exchange. If we assume spherical symmetry and radial flow, the equation 4.30 reduces to equation 4.6.

4.3 The equation of motion

The equation of motion for particle species s, from *Janse et al.* (2005) is

$$n_s m_s \frac{D\mathbf{u_s}}{Dt} + \nabla \cdot \underline{\underline{\mathbf{P_s}}} - n_s m_s \mathbf{G} - n_s e_s (\mathbf{E} + \mathbf{u_s} \times \mathbf{B}) = \frac{\delta \mathbf{M_s}}{\delta t}, \tag{4.31}$$

where $\frac{D}{Dt} = \frac{\partial}{\partial t} + \mathbf{u_s} \cdot \nabla$, is the convective derivative, $\mathbf{P_s}$ is the pressure tensor, $\mathbf{G}$ is the gravitational acceleration per particle, $\overline{\overline{\mathbf{B}}}$ is the magnetic field and $\frac{\delta \mathbf{M_s}}{\delta t}$ is the collisional term. If we assume spherical symmetry and radial flow, equation 4.31 reduces becomes

$$\begin{aligned} n_s m_s \frac{\partial u_s}{\partial t} + n_s m_s u_s \frac{\partial u_s}{\partial r} &= -n_s k \frac{\partial T_{s\parallel}}{\partial r} - k T_{s\parallel} \frac{\partial n_s}{\partial r} - \frac{1}{A}\frac{dA}{dr} k n_s (T_{s\parallel} - T_{s\perp}) \\ &\quad + n_s Z_s e E - \frac{n_s G m_s M_\odot}{r^2} + \frac{\delta M_s}{\delta t}, \end{aligned} \tag{4.32}$$

which is the same as equation 4.8.

The convective derivative of the momentum, the two terms on the left hand side of equation 4.32, describes the change in momentum with time, in a frame moving with the fluid. The first two terms on the right hand side of equation 4.32 describes the pressure gradient force owing to the pressure in the direction parallel to the magnetic field. The third term on the right hand side contains the perpendicular pressure. As we will show later in this section, a pressure applied in the perpendicular direction will affect the flow of momentum in the parallel direction. The fourth and fifth term on the right hand side of equation 4.32 describes the gravitational and electric field force, respectively. The electric field set up by the proton-electron background is calculated from the equation of motion for the electrons by assuming $n_e = n_p$ and $u_e = u_p$, i.e. no current ($j = e(n_p u_p - n_e u_e)$).
The last term is the collisional term, given by equation 4.33 (same as equation 4.9),

$$\begin{aligned} \frac{\delta M_s}{\delta t} &= -\sum_t n_s m_s \nu_{st} (u_s - u_t) \\ &+ \sum_t \nu_{st} \frac{3}{5} \frac{\mu_{st}}{k T_{st}} \left[q_s \left(1 - \frac{5}{7} \frac{m_t}{m_s + m_t} \right) - q_t \frac{m_s n_s}{m_t n_t} \left(1 - \frac{5}{7} \frac{m_s}{m_s + m_t} \right) \right] \\ &+ m_s \sum_t (n_t u_t R_{ts} - n_s u_s R_{st}) \end{aligned} \tag{4.33}$$

The collisional term describes the friction force caused by collisions with particles of other species (first term on the right hand side), and the thermal force (second term on the right hand side). The last term describes the change in momentum as a result of ionization, recombination and charge exchange. This term is present in the equations for the numerical model, but not in the equations developed by *Janse et al.* (2005). Again, this is because the equations of *Janse et al.* (2005) describe fully ionized gases.

The Coulomb collision frequency between particles of species s and t is proportional to $(\mathbf{v_s} - \mathbf{v_t})^{-4}$, where $\mathbf{v} = \mathbf{u} + \mathbf{c}$, $\mathbf{u}$ is the mean velocity of the particles, and $\mathbf{c}$ is a random thermal velocity. This means that particles

tend to collide with other particles whose velocity is similar to their own. In a fluid description, this energy dependence of the coulomb collision frequency translates into a temperature dependency in the collision frequency, and a net force on the particles, called the thermal force, which depends on the temperature gradient (i.e. on the heat flow, as we can see from equation 4.33). From the expression for the collision frequency in equation 4.12, we see that the collision frequency is proportional to ${T_{st}}^{-3/2}$. Owing to their larger mass, the protons in the transition region have a thermal velocity, $v_{th} = (kT/m)^{1/2}$, which is much lower than the thermal velocity of the electrons (the temperatures of protons and electrons are assumed to be equal). Thus, the heavy protons can be assumed to be at rest, relative to the electrons. Owing to the temperature-dependence of the collision frequency, the protons in the transition region will collide more often with the slow, upward-moving electrons below them, where the temperature is low, than with the faster, downward-moving electrons above them, where the temperature is high. The result is a net upwards force on the protons, i.e. in the direction of increasing temperature. This force must be paired with an equal, but oppositely directed force on the electrons. Since collisions between cold, upward-moving electrons, and protons at rest above them, (corresponding to a downward force on the electron fluid) are more frequent than collisions between hot, downward-moving electrons, and protons at rest below them, (corresponding to an upward force on the electron fluid), the total force on the electrons fluid must be directed downwards, i.e. in the direction of decreasing temperature. In regions of large temperature gradients, the thermal force can become significantly larger than gravity. For heavy minor ions, colliding with lighter protons and electrons, the thermal force is also directed towards increasing temperatures in the transition region. Because of the low abundances of the minor ions, the force per particle on the minor ions, is much larger than the oppositely directed force per particle on the protons and electrons.

To obtain equation 4.32 we must find the divergence of the pressure tensor (second term on the left hand side in equation 4.31). We shall do this by applying Gauss' theorem to a small section of the flow tube, shown in figure 4.2,

$$\int \nabla \cdot \underline{\underline{\mathbf{P}}} dV = \oint \underline{\underline{\mathbf{P}}} \cdot d\mathbf{S} \tag{4.34}$$

The pressure tensor, $\underline{\underline{\mathbf{P}}}$ (we shall skip the subscript s from now on, for easier notation), is assumed to be diagonal in spherical coordinates, i.e.

$$\underline{\underline{\mathbf{P}}} = P_{\parallel} \mathbf{e_r} \mathbf{e_r} + P_{\perp} \mathbf{e}_{\phi} \mathbf{e}_{\phi} + P_{\perp} \mathbf{e}_{\theta} \mathbf{e}_{\theta}, \tag{4.35}$$

where $P_{\parallel/\perp} = nkT_{\parallel/\perp}$, and $\mathbf{e_r}$, $\mathbf{e}_{\phi}$ and $\mathbf{e}_{\theta}$ are the unit vectors in spherical coordinates.

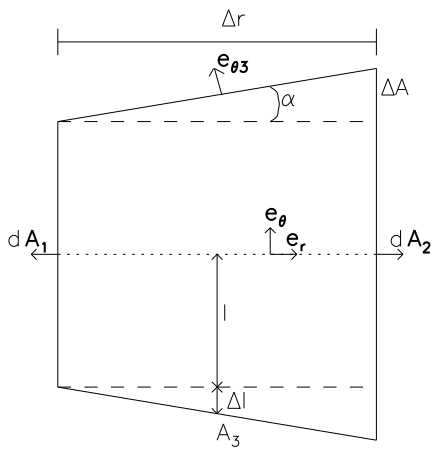

Figure 4.2: Schematic of a small flow tube element of length Δr

We have that

$$\oint \underline{\underline{\mathbf{P}}} \cdot d\mathbf{S} = \int_{A_1} \underline{\underline{\mathbf{P}}} \cdot d\mathbf{A_1} + \int_{A_2} \underline{\underline{\mathbf{P}}} \cdot d\mathbf{A_2} + \int_{A_3} \underline{\underline{\mathbf{P}}} \cdot d\mathbf{A_3}, \tag{4.36}$$

where $d\mathbf{A_1} = -dA_1\mathbf{e_r}$, $d\mathbf{A_2} = dA_2\mathbf{e_r}$, $d\mathbf{A_3} = dA_3\mathbf{e}_{\theta_3}$ and $\mathbf{e}_{\theta_3}$ is the unit vector in θ-direction on the surface A_3.
Calculating the integrals we find that

$$\int_{A_1} \underline{\underline{\mathbf{P}}} \cdot d\mathbf{A_1} = -A_1 P_{\parallel 1}\mathbf{e_r}, \tag{4.37}$$

where we have assumed that $P_\parallel$ is constant on A_1 and is equal to $P_{\parallel 1}$,

$$\int_{A_2} \underline{\underline{\mathbf{P}}} \cdot d\mathbf{A_2} = A_2 P_{\parallel 2}\mathbf{e_r}, \tag{4.38}$$

where we have assumed that $P_\parallel$ is constant on A_2 and is equal to $P_{\parallel 2}$, and

$$\int_{A_3} \underline{\underline{\mathbf{P}}} \cdot d\mathbf{A_3} = \int_{A_3} P_{\perp 3} dA_3 \mathbf{e}_{\theta_3}, \tag{4.39}$$

where $P_{\perp 3}$ is the perpendicular pressure at the surface A_3.
The assumptions above, that $P_\parallel$ is constant on A_1 and on A_2 are necessary because we integrate over the cross-sectional area of the flow tube, and not over the surface $\Omega_{FT} r^2$, where Ω_{FT} is the solid angle of the flow tube.
The unit vector $\mathbf{e}_{\theta_3}$ can be expressted in terms of the unit vectors in the radial and θ-direction at the center of the flow-tube element, $\mathbf{e_r}$ and $\mathbf{e}_\theta$,

$$\mathbf{e}_{\theta_3} = \cos\alpha \mathbf{e}_\theta - \sin\alpha \mathbf{e_r}, \tag{4.40}$$

We can also write $P_{\perp 3}$ as

$$P_{\perp 3} = P_\perp + \frac{dP_{\perp 3}}{dr} \cdot dr, \tag{4.41}$$

where $P_\perp$ is the perpendicular pressure on the surface A_3 at the bottom of the flow tube element and $\frac{dP_{\perp 3}}{dr}$ is assumed to be constant. Using $dA_3 = 2\pi l dr$ and equations 4.40 and 4.41 we find

$$\begin{aligned}\int_{A_3} P_{\perp 3} dA_3 \mathbf{e}_{\theta \mathbf{3}} &= \textstyle\int_{A_3} P_{\perp 3} dA_3 \cos\alpha \mathbf{e}_\theta - \int_{A_3} P_{\perp 3} dA_3 \sin\alpha \mathbf{e_r} \\ &= -\textstyle\int_{\Delta r} \left(P_\perp + \frac{dP_{\perp 3}}{dr} \cdot dr\right) 2\pi l dr \sin\alpha \mathbf{e_r} \\ &= -P_\perp 2\pi l \Delta r \sin\alpha \mathbf{e_r}, \end{aligned} \tag{4.42}$$

since $\frac{dP_{\perp 3}}{dr} 2\pi l dr^2$ is a second order term, and the term $\int_{A_3} P_{\perp 3} dA_3 \mathbf{e}_\theta \cos\alpha$ vanishes because of symmetry.
By noting that $\sin\alpha \simeq \Delta l/\Delta r$ and that $2\pi l \Delta l = A_2 - A_1 = \Delta A$, we find that

$$2\pi l \Delta r \sin\alpha = \Delta r \frac{\partial A}{\partial r}, \tag{4.43}$$

which finally gives us

$$\int_{A_3} \underline{\underline{\mathbf{P}}} \cdot d\mathbf{A_3} = -P_\perp \Delta r \frac{\partial A}{\partial r} \mathbf{e_r}. \tag{4.44}$$

Now, we are ready to use equation 4.34 to find an expression for $\nabla \cdot \underline{\underline{\mathbf{P}}}$.
We have that

$$\int_V \nabla \cdot \underline{\underline{\mathbf{P}}} dV = \nabla \cdot \underline{\underline{\mathbf{P}}} \int_{\Delta r} A dr = \nabla \cdot \underline{\underline{\mathbf{P}}} A \Delta r, \tag{4.45}$$

where we have assumed that $\nabla \cdot \underline{\underline{\mathbf{P}}}$ is constant in the volume $A\Delta r$. This gives us

$$\nabla \cdot \underline{\underline{\mathbf{P}}} A \Delta r = \mathbf{e_r} \left[P_{\parallel 2} A_2 - P_{\parallel 1} A_1 - P_\perp \Delta r \frac{\partial A}{\partial r} \right], \tag{4.46}$$

or,

$$\begin{aligned}\nabla \cdot \underline{\underline{\mathbf{P}}} = \quad & \mathbf{e_r} \left(\tfrac{1}{A} \tfrac{\partial}{\partial r} (A P_\parallel) - P_\perp \tfrac{1}{A} \tfrac{\partial A}{\partial r} \right) \\ = & \mathbf{e_r} \left(\tfrac{\partial P_\parallel}{\partial r} + \tfrac{1}{A} \tfrac{\partial A}{\partial r} (P_\parallel - P_\perp) \right) \end{aligned} \tag{4.47}$$

By substituting $nkT_{\parallel/\perp}$ for $P_{\parallel/\perp}$ we see that the expression inside the parentheses in equation 4.47 is identical to the first three terms on the right hand side of equation 4.32.

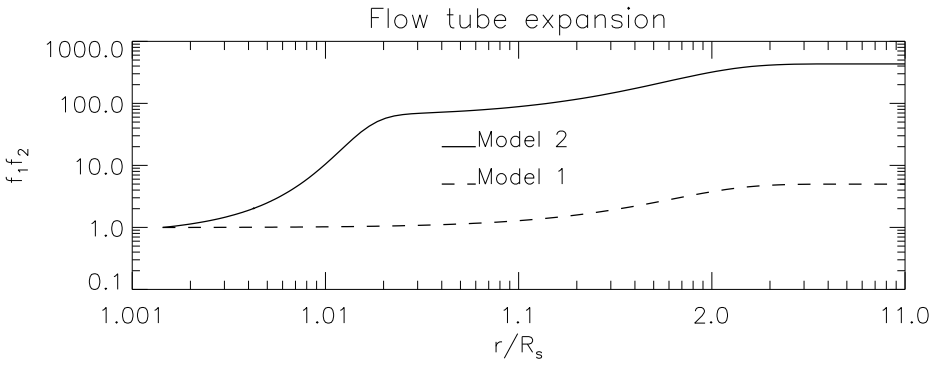

Figure 4.3: Expansion of the flow tube in Model 1 and Model 2 as a function of radial distance from the solar center.

4.4 Solving the equations

We assume that the abundances of the minor ions are too low for them to be able to affect the major species, i.e. the hydrogen/proton/electron background, and the minor species are treated as test particles that flow in a fixed background. In our simulations for the minor ions, the ratio of the total densities of the minor species (oxygen, neon, carbon or magnesium) to the major species (hydrogen/protons), $n_{el}/(n_p + n_H)$, never exceeds $2 \cdot 10^{-3}$. Two background models have been calculated from equations 4.6 to 4.26. The background models that we have used are the same as those presented in *Esser et al.* (2005). They are both able to produce a solar wind at 1 AU that is consistent with observations, but Model 2 is in better agreement with observations of the corona than Model 1. The background models are characterized primarily by their geometry. We have chosen two rather extreme cases (see description below). The lower boundary of both background models is in the chromosphere, where the density is about $1.7 \cdot 10^{17} m^{-3}$, and the electron temperature is 7270 K.

4.4.1 The background models

The expansion of the flow tube in the two models, given by $f_1(r)f_2(r)$, is plotted in figure 4.3 as a function of distance from the solar surface, in the range $1.001R_\odot$-$11R_\odot$.

The first background model, Model 1, has a "classical"(e.g. *Munro and Jackson*, 1977) coronal hole expansion, and the second, Model 2, has a funnel type expansion (e.g. *Tu et al.*, 2005). For Model 1 we use $f_{max1} = 1$ with $R_{11} = 1.015$ and $f_{max2} = 5$ with $R_{12} = 1.3$. For Model 2 we use $f_{max1} = 62$ with $R_{11} = 1.015$ and $f_{max2} = 7$ with $R_{12} = 1.3$. The cross sectional area of the flow tube at the lower boundary of the model, A_0, is 1 m^2 for both

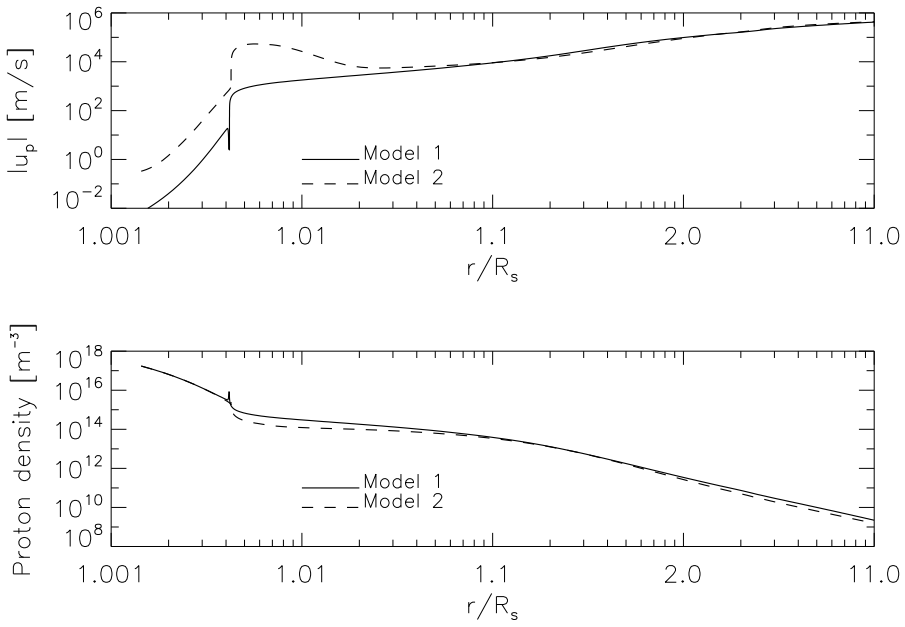

Figure 4.4: Proton flow velocity and density for the two background models, plotted vs. radial distance from the solar center.

background models. (See section 4.1, equations 4.27 to 4.29.)

In the solar atmosphere, a total energy flux of 188 J/s, is deposited in the proton fluid in Model 1. In Model 2 the total energy flux deposited in the protons in the solar atmosphere is increased to $5.9{\cdot}10^5$ J/s. The protons are only heated in the perpendicular direction. The electrons are heated by an energy flux of 557 J/s in Model 1 and 4500 J/s in Model 2, and are heated isotropically. In the extended corona and solar wind, energy is also added to the proton-electron fluid by Alfvén waves, through the Alfvén wave pressure gradient force (see section 2.3). The heating parameters have been chosen such that they produce a solar wind that is in relatively good agreement with observed values in the corona and at 1 AU.

The proton densities and flow velocities for the two background models are plotted in figure 4.4. The flow velocity in the transition region for Model 1 is low, but increases to about 10-20 km/s in the upper transition region/lower corona. The flow velocity in Model 2 is much higher than in Model 1 in the transition region, below $1.02R_\odot$. This is because of the large expansion of the flow tube in Model 2 in this region (see figure 4.3). The large expansion of the flow tube leads to a decrease in density, which must be matched by an increase in flow velocity, to keep the mass flux constant. In the upper transition region/lower corona, above $1.02R_\odot$, the flow velocity

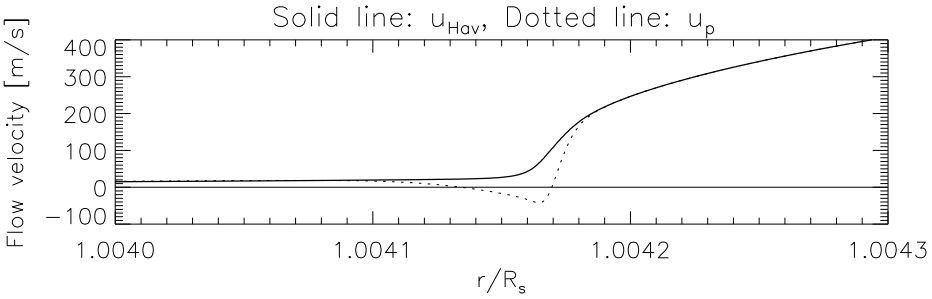

Figure 4.5: Average flow velocity of hydrogen (u_{Hav}), and flow velocity of protons in Model 1, plotted vs. radial distance from the solar center, in the range 1.004-1.0043$R_\odot$. This corresponds to the temperature range from $8.6 \cdot 10^3$ K to $1.1 \cdot 10^5$ K.

in Model 2 is much lower, and closer to that in Model 1.

In Model 1, there is a spike in the flow velocity in the transition region, just above 1.004$R_\odot$. In this small region, the proton flow velocity becomes negative, and the protons stream down towards the sun. Hydrogen continues to flow outwards throughout this narrow region, and the average hydrogen flow velocity, $u_p n_p + u_H n_H/(n_p + n_H)$, is positive, as we can see in figure 4.5, where we have plotted the average hydrogen flow velocity and the proton flow velocity in the height region 1.004-1.0043$R_\odot$. In Model 1, the protons and electrons that form the solar wind are those that escape as neutral hydrogen in the region where the flow velocity of the protons is negative.

The region where the proton flow velocity is negative corresponds to the region where most of the neutral hydrogen is being ionized. We can see this as a rapid increase in density in the bottom panel of figure 4.4. This rapid increase in density, together with increasing temperature, gives rise to a large negative (in this context, a negative force is directed down towards the solar surface, i.e. negative radial direction) pressure gradient force, which pulls the proton-electron fluid down towards the sun.

The forces acting on the proton-electron fluid in the region 1.004$R_\odot$ to 1.0043$R_\odot$ are plotted in figure 4.6. The dominant forces are the negative pressure gradient force, and the positive force resulting from charge exchange between protons and hydrogen. The third force is the Alfvén wave pressure gradient force (discussed in section 2.3). As we noted in section 2.3, the energy transferred to the plasma through the Alfvén wave pressure gradient force is small when the product $\mathbf{u} \cdot \nabla \mathbf{P}_{Aw}$ is small. In the lower transition region, the flow velocity is very low, less than 0.4 km/s (see figure 4.5), and thus, the Alfvén wave energy flux density (Alfvén wave Poynting flux) at these heights is approximately constant, and proportional to $\partial B^2 \cdot v_A$, where $v_A = B/(\mu_0 \rho)^{1/2}$ is the Alfvén speed. Since $\partial B^2 \cdot v_A$ is constant,

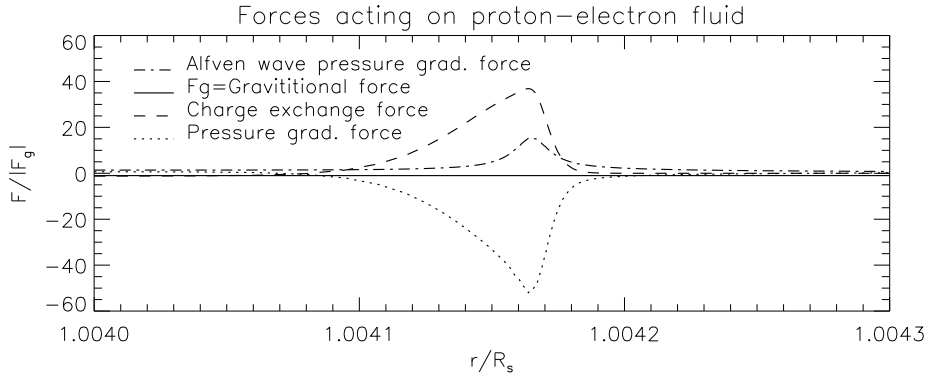

Figure 4.6: Forces acting on the proton-electron fluid, plotted vs. radial distance from the solar center, in the range 1.004-1.0043$R_\odot$. This corresponds to the temperature range from $8.6 \cdot 10^3$ K to $1.1 \cdot 10^5$ K.

and $v_A \propto (1/n)^{1/2}$, ∂B must increase in regions of rapidly increasing proton density. When the proton density increases in the lower transition region, as a result of ionization of hydrogen, the wave pressure gradient force, i.e. $\nabla \mathbf{P}_{Aw}$, which is otherwise negligible at these heights, becomes comparable to the other forces acting on the protons, in a small height region.

The proton and electron temperatures for the two background models are plotted in figure 4.7. Both the electron and proton temperatures are larger in Model 2 than in Model 1 in the transition region.

4.4.2 The minor ions

For the minor ions we solve equation 4.6 to 4.19, using the two background models. The equations are solved for all the minor ion charge states simultaneously. We did not solve the heat flow equation for the minor ions because the heat flow of the minor ions is negligible.

Since we do not really know how the minor ions are heated, or how much, we can choose the heating parameters freely, as long as they are able to produce minor ion flow velocities and temperatures that are reasonable, and in relatively good accordance with observations, where observational results are available. The minor ions are heated with an energy flux per particle that varies with the distance to the solar center as described by the heating function.

The heating function for the minor ions is shown in figure 4.8. The heating is increased linearly from zero to its maximum value, over a distance R_{heat} to $R_{heat} + \Delta R$ from the solar center. This is mainly done to avoid problems with the numerical calculations, that might arise if we were to switch the heating on very suddenly. In figure 4.8, $R_{heat} = 1.4R_\odot$ and $\Delta R = 0.4R_\odot$. When the heating function has reached its maximum value,

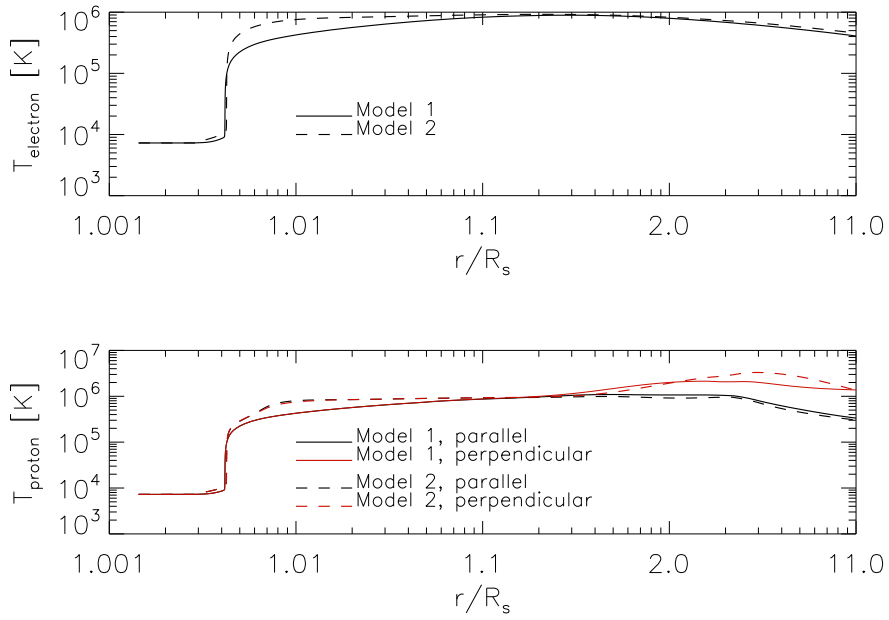

Figure 4.7: Electron and proton temperatures for the two background models, plotted vs. radial distance from the solar center.

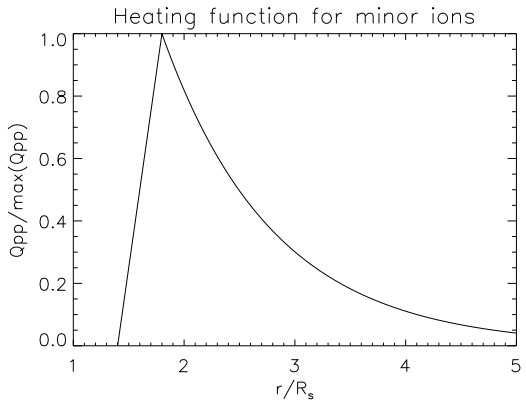

Figure 4.8: Heating function for the minor ions, plotted vs. radial distance from the solar center. Qpp is the heating rate per particle.

it is decreased exponentially with a damping length of R_{damp}. In figure 4.8 the damping length is $R_{damp} = 1R_{\odot}$. The code also allows for different values of the heating per particle in the parallel and perpendicular direction.

Chapter 5

Results

In this chapter we shall present the results of the simulations done for the six minor ion species and the two background models. For oxygen, we present results from one set of heating parameters, found to produce temperature- and velocity profiles for O^{5+} which are in agreement with observations. In a study using in-situ observations of the particle velocity distributions of several charge states of neon, carbon, oxygen and magnesium, *von Steiger et al.* (1995) found that the temperatures of these ions obeyed the relation $T_i/T_j \simeq m_i/m_j$. Similar results have been obtained through off-limb spectroscopic observations of a polar coronal hole by *Tu et al.* (1998) and *Tu et al.* (1999). Based on these results, we have chosen to heat the ions of neon, carbon and magnesium mass proportionally with respect to the heating rates applied to oxygen, i.e., $max(Qpp)_{el} = max(Qpp)_O(m_{el}/m_O)$. The largest observed minor ion blue-shifts are found in the Ne VIII line, which is consequently blue-shifted in all the studies presented in chapter 3, and which is also the best documented of the ionic emission lines. A theoretical model of the solar transition region should therefore be able to reproduce high outflow velocities for this ion. As we will see later in this chapter, mass proportional heating rates cannot produce outflow velocities for Ne^{7+} larger than 7.5 km/s. To increase the outflow velocity in the transition region we can either change the background model, or add more energy to the minor ion fluid, by applying larger heating rates. As we shall discuss further in section 6.3, moderate changes in the heating rates for the minor ions do not affect the flow velocity in the transition region. The effect of large heating rates, on Ne^{7+}, will be explored in section 5.2.2.

5.1 Oxygen

We have calculated oxygen flow speeds for several different sets of heating rates (with max(Qpp)$\parallel$ and max(Qpp)$\perp$ ranging from 1-7$\cdot 10^{-18}$J/s) and heating distances (we have used either $R_{heat} = 1.4R_\odot$ or $R_{heat} = 1.5R_\odot$).

All charge states have the same heating rates.

The two sets with the best fit to observed values of the O^{5+} temperature and outflow speed are summarized in table 5.1

Set	max(Qpp)$\parallel$ [10^{-18} J/s]	max(Qpp)$\perp$ [10^{-18} J/s]	R_{heat}	R_{damp}	ΔR
1	1	3	1.4	1	0.4
2	1	3	1.5	1	0.4

Table 5.1: Two different sets of heating parameters used for the calculations for oxygen. Qpp$\parallel$ (Qpp$\perp$) is the parallel (perpendicular) heating rate per particle, corresponding to $\frac{Q_{sm\parallel}}{n_s}$ ($\frac{Q_{sm\perp}}{n_s}$) in equation 4.16 (4.17) in section 4.1. For a detailed description of the parameters R_{heat}, R_{damp}, ΔR and the heating of the minor ions see section 4.4.2.

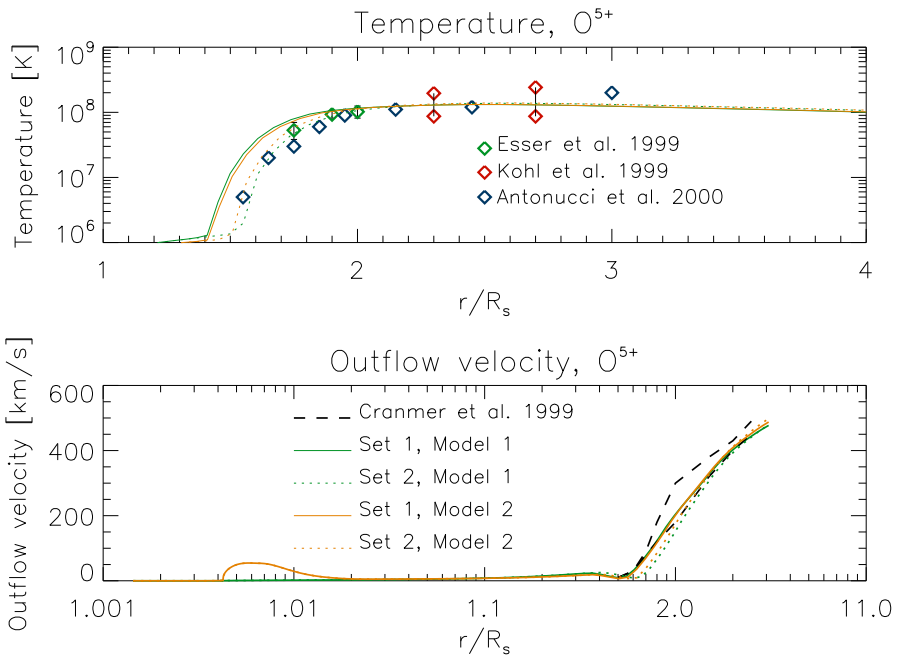

Figure 5.1: Observed and calculated temperatures (top panel, plotted vs. radial distance from the solar surface, on a linear axis) and outflow velocities (bottom panel, plotted vs. radial distance from the solar surface, on a logarithmic axis) for O^{5+}, Model 1.

The top panel in figure 5.1 shows the calculated O^{5+} temperatures for the two sets in table 5.1 and for both background models, together with O^{5+} temperatures deduced from observations from three different authors. In the bottom panel we have plotted the calculated O^{5+} outflow velocities

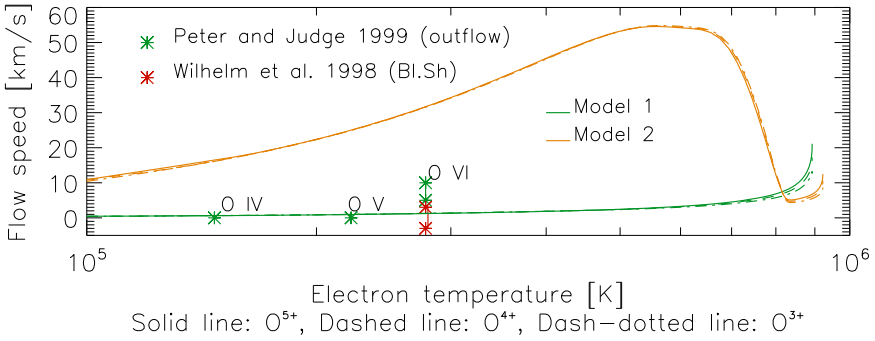

Figure 5.2: Comparison of observed and calculated outflow velocities for three oxygen ions, plotted vs. electron temperature, set 1, Model 1,2. Note: The measured blue-shifts/estimated outflow from observations are plotted at the ionization equilibrium formation temperature. At this temperature the calculated flow velocities in Model 2 are not very high, however, at the formation temperatures obtained for Model 2, the flow velocities have increased to higher values. For Model 1, the calculated formation temperatures more or less coincide with the ionization equilibrium temperatures.

(solid lines) compared with observed O^{5+} outflow velocity (dashed lines, indicating upper and lower bound). O^{5+} is the only oxygen ion for which observations of outflow and temperature profiles in the corona exists. The set that best fits the observed O^{5+} temperature profile is set 2, and the set that best fits the observed O^{5+} outflow velocity profile is set 1. Since we are primarily interested in the outflow velocities, we have used the results from set 1 in the following analysis.

Figure 5.2 shows the observed flow velocities of O^{3+}, O^{4+} and O^{5+} at the formation temperatures obtained when assuming ionization equilibrium together with the calculated flow velocities of O^{3+}, O^{4+} and O^{5+}, for both models. The flow velocities obtained with Model 1 are in agreement with the observations of *Wilhelm et al.* (1998), and with the observations for O^{3+} and O^{4+} from *Peter and Judge* (1999). *Peter and Judge* (1999) found higher outflow velocities for O^{5+}, but for Model 1 we find low outflow velocities for all three ions. These three oxygen ions are all formed below $1.01R_{\odot}$. We start to heat the minor ions at $1.4R_{\odot}$. Since we do not heat the ions in the region where they are formed, changing the heating rates will not lead to changes in the outflow velocities at the formation temperature. If we were to heat the ions in the formation region (i.e. decrease R_{heat} with respect to the values in table 5.1), we would not be able to produce O^{5+} temperatures above $1.2R_{\odot}$, in agreement with observations. The effect of changing the heating distance, R_{heat}, can be seen in figure 5.1 (top panel), where the

temperature profiles for set 1 are shifted towards lower heights compared to the temperature profiles for set 2. For the set we have used in figure 5.2 (set 1), the temperature profile is already shifted towards lower heights compared to the observed temperature profile. A further decrease in the heating distance would lead to even larger discrepancies with the observed values for the O^{5+} temperature. In addition, the minor ions are very well coupled to the protons in the transition region, and the minor ion flow velocities here will not respond to moderate changes in the heating rates (this will be demonstrated in section 6.3).

For Model 2, the calculated flow velocity is much higher than the observed values, for all three ions. This is because the proton flow velocity in this region is much higher in Model 2. For oxygen, it is clear that the outflow velocities obtained with Model 1 are in better agreement with observations than the those obtained with Model 2.

5.1.1 Model 1

In figure 4.4 (section 4.4.1), we saw that in Model 1, just above $1.004R_\odot$, there is a negative spike in the proton flow velocity, corresponding to a region where the protons flow downwards. The proton flow velocity in this region is shown in the top panel of figure 5.3, together with the average flow velocity of oxygen ($u_O = \sum_{i=0}^{8} u_{O^{i+}} \cdot x_i$), as a function of electron temperature, in the range 10^4K to 10^5K. This electron temperature range covers the height region from about $1.00415R_\odot$ to $1.00425R_\odot$. The dominant ionic charge states of oxygen in this height region are neutral oxygen, O^{1+} and O^{2+}. The average flow velocity of oxygen is positive throughout the region where the protons flow downwards, just as the average flow velocity of hydrogen, i.e. $u_p n_p + u_H n_H/(n_p + n_H)$, is positive throughout this region (see figure 4.5, section 4.4.1). The oxygen flow velocity differs somewhat from the proton flow velocity, but the difference is not very large, less than 0.2 km/s.

The bottom panel in figure 5.3 shows the ratio between the average flow velocity of oxygen and the proton flow velocity, u_O/u_p. In the region between $3 \cdot 10^4$K and $4 \cdot 10^4$K, there is a large peak in u_O/u_p. This peak occurs because the flow velocity of the protons changes from negative to positive values. When the proton flow velocity crosses zero, the rather small difference in flow velocity between oxygen and protons causes a large peak in u_O/u_p.

Figure 5.4 shows the ion fractions (top panel) together with u_i/u_p (bottom panel) for $i = O^{3+}$, O^{4+} and O^{5+} in the electron temperature range from 10^5K to 10^6K. In the region where these ions are dominant, the flow velocity of the oxygen ions can deviate from the proton flow velocity by up to 20%. However, the proton flow velocity is low in this temperature range for Model 1, and the relative flow velocity between these oxygen ions and protons is still less than 0.2 km/s.

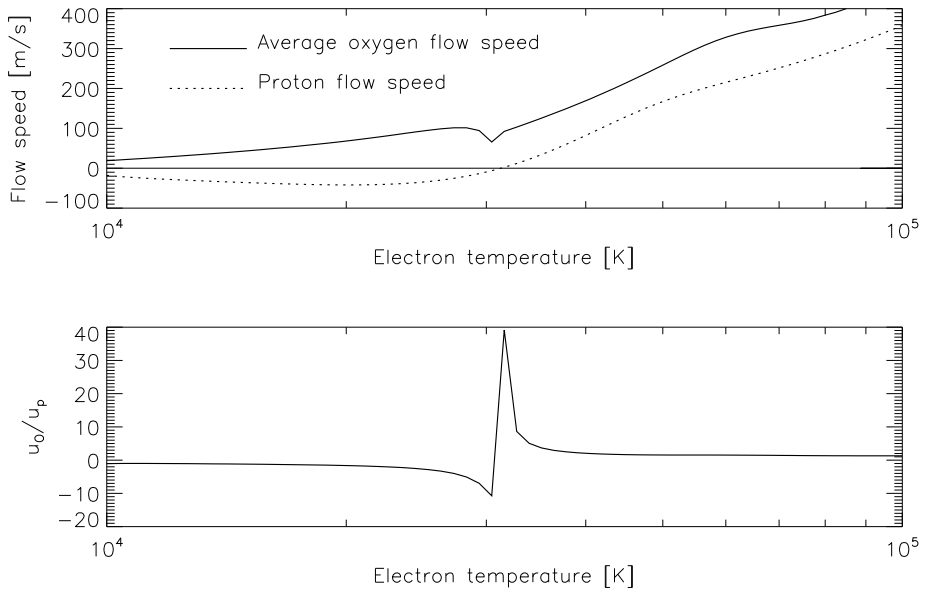

Figure 5.3: Flow velocity of protons together with average flow velocity of oxygen (top panel) and u_O/u_p (bottom panel) in the transition region, plotted vs. electron temperature in the range 10^4K to 10^5K, set 1, Model 1.

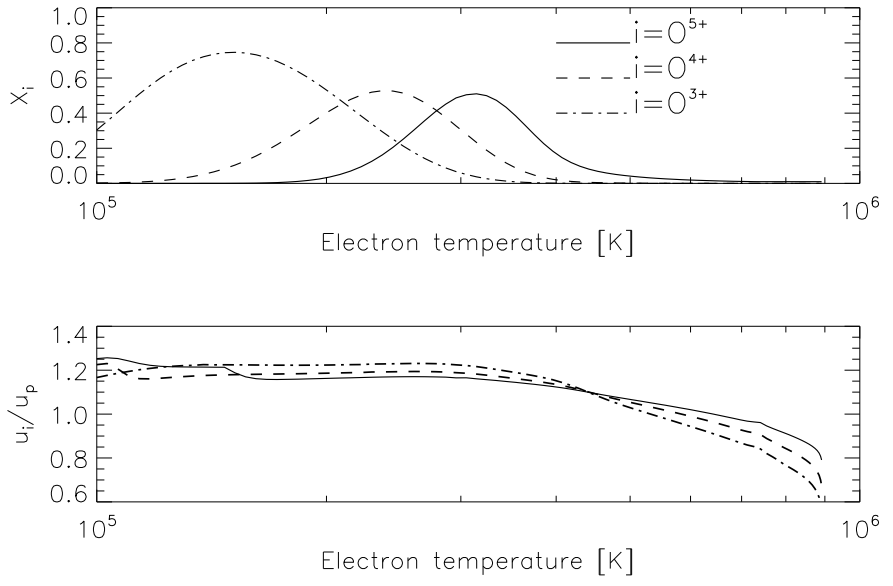

Figure 5.4: Ion fractions for O^{3+}, O^{4+} and O^{5+} (top panel) and u_i/u_p for $i = O^{3+}$, O^{4+} and O^{5+} (bottom panel) in the transition region, plotted vs. electron temperature in the range 10^5K to 10^6K, set 1, Model 1.

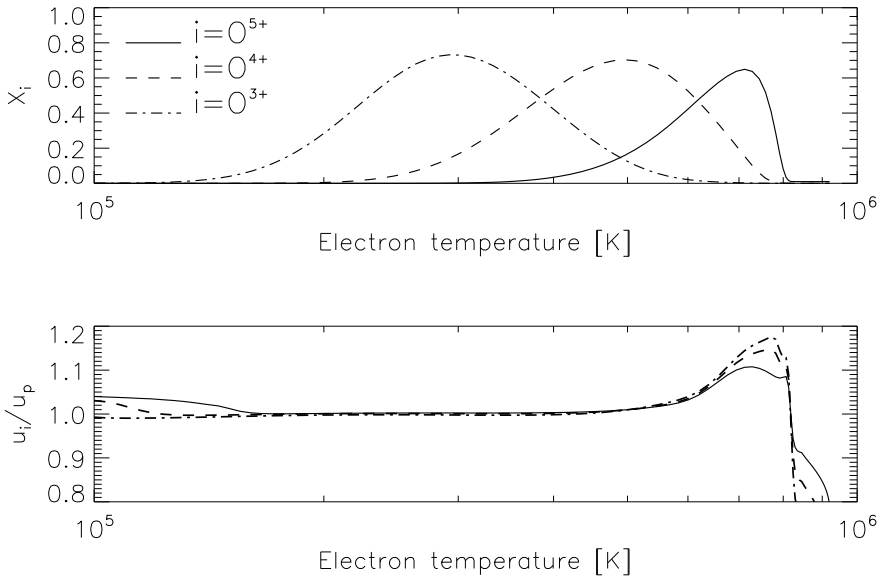

Figure 5.5: Ion fractions for O^{3+}, O^{4+} and O^{5+} (top panel) and $u_{O^{3+}}/u_p$,$u_{O^{4+}}/u_p$ and $u_{O^{5+}}/u_p$ (bottom panel) in the transition region, plotted vs. electron temperature in the range 10^5K to 10^6K, set 1, Model 2.

The collision frequency of an oxygen ion, of charge e_s, with protons (or electrons), and thereby the thermal force (for a description of the thermal force, see section 4.3), is proportional to the charge of the ions squared, ${e_s}^2$ (see equation 4.12, in section 4.1). Since the temperature is approximately the same for all the oxygen species in this height range, and the heat flux for minor ions is negligible, the thermal force is given by the background and only varies in magnitude between the different charge states of oxygen. The same is true for the electric field force, which is proportional to e_s (for a description of the electric field, see equation 4.12, in section 4.3). The pressure gradient force and the frictional force are the only forces that are completely unique for each oxygen species. If the pressure gradient force did not vary between different oxygen species, the flow velocity profiles for the different species should also be identical, except in magnitude (owing to the charge dependency of the thermal and electric forces). Any additional variations between the flow velocity profiles of the different charge states are attributable to variations in the pressure gradient force, caused by variations in the individual densities.

5.1.2 Model 2

In Model 1 there was a peak in u_O/u_p in a region where the proton flow velocity was very small, just as it changed from negative to positive values (figure 5.3). In Model 2, the flow velocity in the transition region is much higher (see figure 4.4 in section 2) than in Model 1, and it is positive throughout the electron temperature range from 10^4K to 10^5K. Therefore, we do not find a large peak in u_O/u_p in this region, for Model 2.

Figure 5.5 shows the ion fractions (top panel) together with u_i/u_p (bottom panel) for $i = O^{3+}$, O^{4+} and O^{5+}, in the electron temperature range from 10^5K to 10^6K. For all three ions, u_i/u_p is between 1 and 1.2 in the region of maximum ion fraction. In Model 2, the flow velocity is very high at these temperatures, and the O^{5+} ions are faster than the protons by 4.26 km/s. For O^{3+} and O^{4+}, the relative flow velocity with respect to the protons is less than 0.5 km/s. The maximum of the ion fractions is shifted in temperature, towards higher temperatures in Model 2, compared with Model 1. The maximum of the ion fractions in Model 1 more or less coincide with the formation temperatures from figure 3.1 (i.e. the ionization equilibrium formation temperatures), but not so for the ion fractions in Model 2. This is because in Model 2, the outflow velocities are so large that oxygen is significantly out of ionization equilibrium.

5.2 Neon

5.2.1 Model 1

For this model we will only present results from one set of heating parameters. The heating parameters used are the same as those in set 1 for oxygen except that the heating rates have been scaled according to mass, i.e. $max(Qpp)_{Ne} = max(Qpp)_O(m_{Ne}/m_O)$

The ionization and recombination processes for minor ions depend primarily on collisions with electrons. When the flow velocity of the minor ions increases, and the electron density falls off as we move outwards from the solar surface, a critical distance is reached, where the timescale for ionization/recombination exceeds the timescale for expansion, and the ionization and recombination of the minor ion species stops. From that point on, the ion fractions are constant, they are frozen into the solar wind. The freezing in distance may differ between different elements, and different ions of the same element.

Figure 5.6 shows the Ne^{7+} ion fraction (top panel) and the Ne^{7+} to proton flow speed ratio (middle panel) in the height range $1.01R_\odot$ to $2R_\odot$. Also plotted is the electron temperature as a function of height. The dominant charge states of neon in this temperature/height region are Ne^{7+} and Ne^{8+}. In the region where Ne^{7+} is a dominant charge state, these ions are well

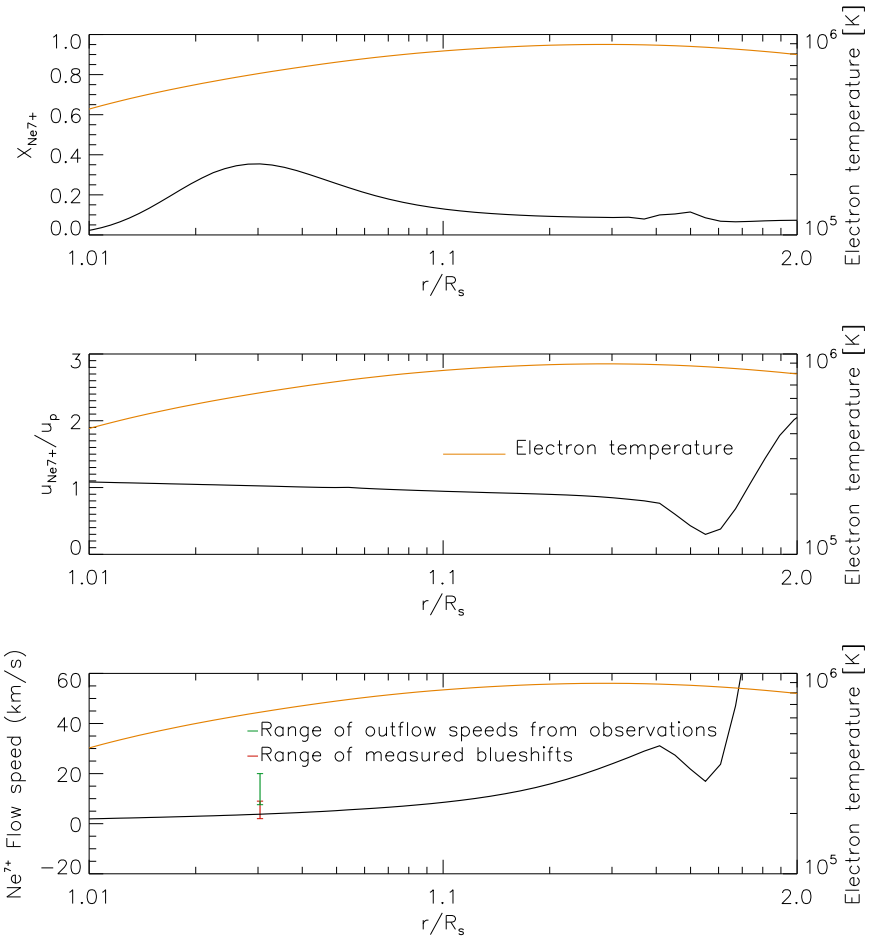

Figure 5.6: Ne^{7+} ion fraction (top panel), $u_{Ne^{7+}}/u_p$ (middle panel) and Ne^{7+} outflow velocity (bottom panel), plotted vs. radial distance from the solar center, Model 1.

coupled to the protons. The freezing in distance is reached at about $1.7R_\odot$. Above the freezing in distance, the Ne^{7+} ions are decoupled from the background. The ion fraction of Ne^{7+} is very small above the freezing in point, and we expect that the contribution from this region, to the Doppler-shift in the Ne VIII emission line, will be insignificant. In the bottom panel we have plotted the Ne^{7+} outflow velocity. The range of measured blue-shifts and estimated outflow velocities, shown in figure 3.1, is also indicated. The calculated formation temperature coincides with the formation temperature obtained when assuming ionization equilibrium. The calculated outflow velocity at the point of maximum ion fraction for Model 1 falls within the range of measured blue-shifts.

Set	max(Qpp)$\parallel$ [10^{-18} J/s]	max(Qpp)$\perp$ [10^{-18} J/s]	R_{heat}	R_{damp}	ΔR
1	1.26	3.78	1.4	1	0.4
2	1.26	3.78	1.002	1	0.4
3	1260	3780	1.002	1	0.4
4	80	250	1.002	0.1	0.02

Table 5.2: Four different sets of heating parameters used for the calculations for neon with the Model 2 background. Qpp$\parallel$ (Qpp$\perp$) is the parallel (perpendicular) heating rate per particle, corresponding to $\frac{Q_{sm\parallel}}{n_s}$ ($\frac{Q_{sm\perp}}{n_s}$) in equation 4.16 (4.17) in section 4.1. For a detailed description of the parameters R_{heat}, R_{damp}, ΔR and the heating of the minor ions see section 4.4.2.

5.2.2 Model 2

For Model 2 we shall present the results from four different sets of heating parameters, listed in table 5.2.

The top panel of figure 5.7 shows the ion fraction of Ne^{7+}. As we can see from this figure, the formation region of Ne^{7+} lies between $1.01R_\odot$ and $1.03R_\odot$ for sets 1 and 2 (the ion fraction for set 2 is exactly equal to that for set 1 for the greater part of the temperature/height region shown in figure 5.7). For sets 3 and 4, the Ne^{7+} ions exist over an extended temperature/height region. In set 1, all the heat is deposited above the formation region. In set 2 we have heated the ions very close to the sun, but we have not changed the maximum heating rate, with respect to set 1. The heating rate is increased linearly over $0.4R_\odot$ from where we start to heat, so the amount of heat deposited in the formation region of Ne^{7+} for set 2 is very small. In set 3 we have increased the maximum heating rate with respect to set 2, while keeping all other parameters constant. By increasing the maximum heating rate we also increase the amount of heat that is deposited in the transition region. For set 3, the heating rate in the perpendicular direction, at $1.015R_\odot$ is $40.95 \cdot 10^{-18}$J/s. The parallel heating rate at $1.015R_\odot$ is $122.85 \cdot 10^{-18}$J/s. In set 4 we have reduced the damping- and ramp distances, R_{damp} and ΔR, as well as the maximum heating rates with respect to set 3.

The middle panel in figure 5.7 shows the Ne^{7+} to proton flow speed ratio in the height range $1.01R_\odot$ to $11R_\odot$. For set 1, the Ne^{7+} ions are well coupled to the protons below $1.4R_\odot$, which is where we start to heat. The freezing in distance is reached at about $1.7R_\odot$, where the ion fraction settles at 0.06. Above this height, the Ne^{7+} ions are uncoupled from the background. For set 2, the Ne^{7+} ions are well coupled to the protons below the temperature maximum, at $1.3R_\odot$, although we started to heat at $1.002R_\odot$. This result indicates that below the temperature maximum, the

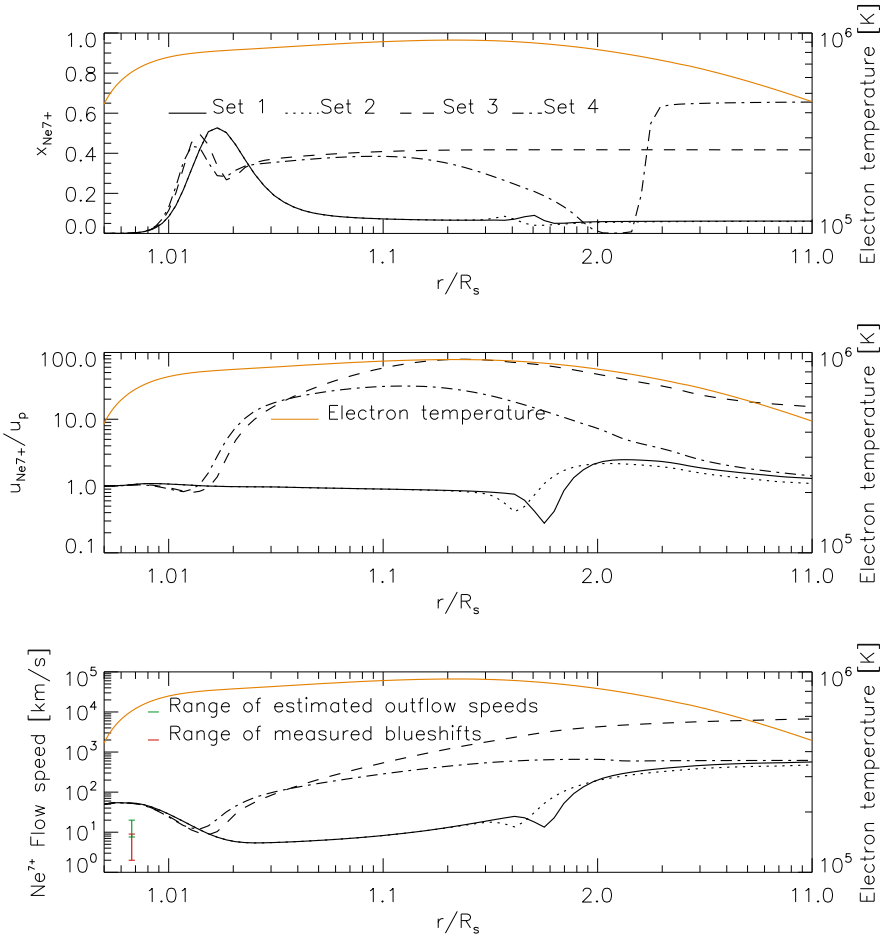

Figure 5.7: Ne^{7+} ion fraction (top panel), $u_{Ne^{7+}}/u_p$ (middle panel) and Ne^{7+} outflow velocity (bottom panel) , plotted vs. radial distance from the solar center, Model 2. Note: The measured blue-shifts/estimated outflow from observations are plotted at the ionization equilibrium formation temperature. At this temperature the calculated flow velocities are very high, however, at the formation temperatures obtained for Model 2, the flow velocities have decreased to lower values.

coupling to the background is strong, and the Ne^{7+} to proton flow speed ratio in this region is not affected by the low heating rates applied in set 2. For set 3, the Ne^{7+} ions are well coupled to the background below about $1.015R_\odot$, where the freezing in distance for the Ne^{7+} ions is reached, and the ion fraction settles at about 0.45. Above the freezing in distance the Ne^{7+} ions are decoupled from the protons. For set 4, the Ne^{7+} ions are also decouple from the protons at about $1.015R_\odot$, but the freezing in distance is reached further out, at about $3R_\odot$. For this set, the dominant charge state in the temperature/height range from about 1.2-2.2$R_\odot$ (the region immediately surrounding the electron temperature maximum) is Ne^{8+}. Just below the freezing in distance, the ion fraction of Ne^{7+} increases, as a result of a decreasing electron temperature. For set 3, the dominant charge states in the solar wind is Ne^{7+}, Ne^{+6} and Ne^{8+} (in that order), and for set 4, Ne^{7+} and Ne^{6+} are dominant.

In the bottom panel of figure 5.7 we have shown the calculated Ne^{7+} outflow velocities in the height range $1.01R_\odot$ to $11R_\odot$ for all four sets. The outflow velocity profile for set 2 is nearly the same as that for set 1. The outflow velocity for set 3 is nearly the same as that for sets 1 and 2 until about $1.015R_\odot$, where the flow velocity for set 3 increases dramatically. The outflow velocity profile for set 4 also follows that of set 1 and 2 until about $1.015R_\odot$, where the flow velocity increases. The flow velocity at $11R_\odot$ for set 3 is very high, above $5 \cdot 10^3$ km/s, but the flow velocity at $11R_\odot$ for set 4 is about the same as that of sets 1 and 2. We have not been able to combine moderate heating rates with a significant increase in the outflow velocity in the formation region.

In the plot showing the outflow velocities for Ne^{7+}, we have also shown the range of measured blue-shifts and estimated outflow velocities, shown in figure 3.1. For Model 2, the ionization equilibrium formation temperature of Ne^{7+} is reached at a lower height than for Model 1. The calculated formation temperatures for Model 2 are higher than the formation temperature obtained when assuming ionization equilibrium. The calculated outflow velocity at the point of maximum ion fraction for sets 1 and 2 falls within the lower part of the range of estimated outflow velocities. The outflow velocity for set 3 is about 2 km/s larger than that for sets 1 and 2. For set 4 the outflow velocity at the point of maximum ion fraction is almost 13 km/s, just below the outflow velocity found by *Peter and Judge* (1999). However, for sets 3 and 4, the region of high outflow above $1.015R_\odot$ may also contribute to the blue-shift of the Ne VIII spectral emission profile, because the Ne^{7+} ions exist over an extended region.

5.3 Carbon

For carbon we have only used one set of heating parameters, which is the same heating parameters as in set 1 for oxygen, except that the ions have been heated mass proportionally, i.e., $max(Qpp)_C = max(Qpp)_O(m_C/m_O)$.

Figure 5.8 shows the ion fraction for C^{3+} (top panel) together with the flow speed ratio of C^{3+} and protons (middle panel), for both models. For Model 1, the C^{3+} flow velocity is between 20% and 40% higher than the proton flow velocity in the region of maximum ion fraction. For Model 2, the flow speed ratio is almost exactly equal to 1 in the formation region. Also shown is the calculated flow velocities for C^{3+}, together with measured blueshifts and estimated outflow velocities at the formation temperatures in table 3.1. The ion fraction maximum is shifted towards higher temperatures for both models, compared to the formation temperature obtained when assuming ionization equilibrium. For Model 2 the shift is large, about $2 \cdot 10^5$K. For Model 1 the calculated flow velocity at the point of maximum ion fraction is near zero, whereas for Model 2 it is very large, about 35 km/s. The calculated outflow velocity for Model 1 agrees with the outflow velocity measured by *Tu et al.* (2005), but not with the other observations. Both *Peter* (1999) and *Peter and Judge* (1999) report outflow velocities that are higher than those obtained with Model 1. For Model 2, the calculated outflow velocities are much higher than any observed outflow velocities. These results are similar to what we saw for oxygen, where we also found large outflow in Model 2, and nearly zero outflow in Model 1, for all three oxygen ions.

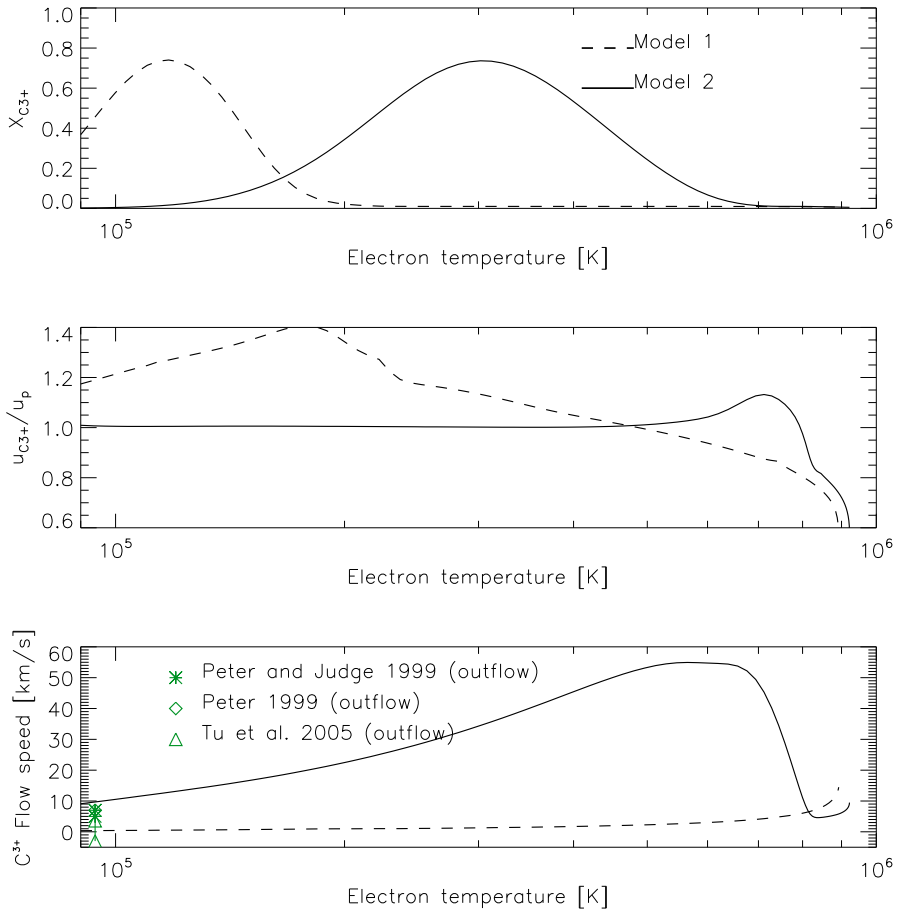

Figure 5.8: C^{3+} ion fraction (top panel), $u_{C^{3+}}/u_p$ (middle panel) and C^{3+} outflow velocity (bottom panel) in the transition region, plotted vs. electron temperature in the range 10^5K to 10^6K, Model 1,2. Note: The measured blue-shifts/estimated outflow from observations are plotted at the ionization equilibrium formation temperature. At this temperature the calculated flow velocity for Model 2 is not very high, however, at the formation temperature obtained for Model 2 the flow velocity has increased to higher values. For Model 1, the calculated formation temperature more or less coincides with the ionization equilibrium temperature.

5.4 Magnesium

To demonstrate the behavior of Mg^{8+}, we shall use the heating parameters in set 1 for oxygen, scaled mass proportionally, i.e.,
$max(Qpp)_{Mg} = max(Qpp)_O(m_{Mg}/m_O)$.

The results are shown in figure 5.9. In the top panel we can see that the Mg^{8+} ions exist over an extended temperature/height range. The Mg^{8+} ions are well coupled to the protons in the region below $1.4R_\odot$, as we can see from the middle panel of figure 5.9, where we have plotted the Mg^{8+} to proton flow speed ratio. The freezing in distance of Mg^{8+} is reached at about $1.7R_\odot$, where $n_{Mg^{8+}}/n_{Mg} = 0.27$. This is in relatively good agreement with *Ko et al.* (1997), who found an average ion fraction for Mg^{8+} of 0.227 for the south polar coronal hole. In the bottom panel of figure 5.9 we have plotted the calculated outflow velocity for Mg^{8+}, together with the measured blue-shift of this ion. The ionization equilibrium formation temperature of Mg^{8+}, is reached at a lower height in Model 2 than in Model 1, therefore we have plotted the measured blue-shift of Mg^{8+} at two different heights.

The Mg^{8+} ions exist over a large range of temperatures. The radiation from this ion probably stems from an extended region in the solar atmosphere. For Model 2, the whole region above $1.01R_\odot$ may contribute to the blue-shift in the emission line of this ion. The outflow velocity of Mg^{8+} varies significantly throughout this region.

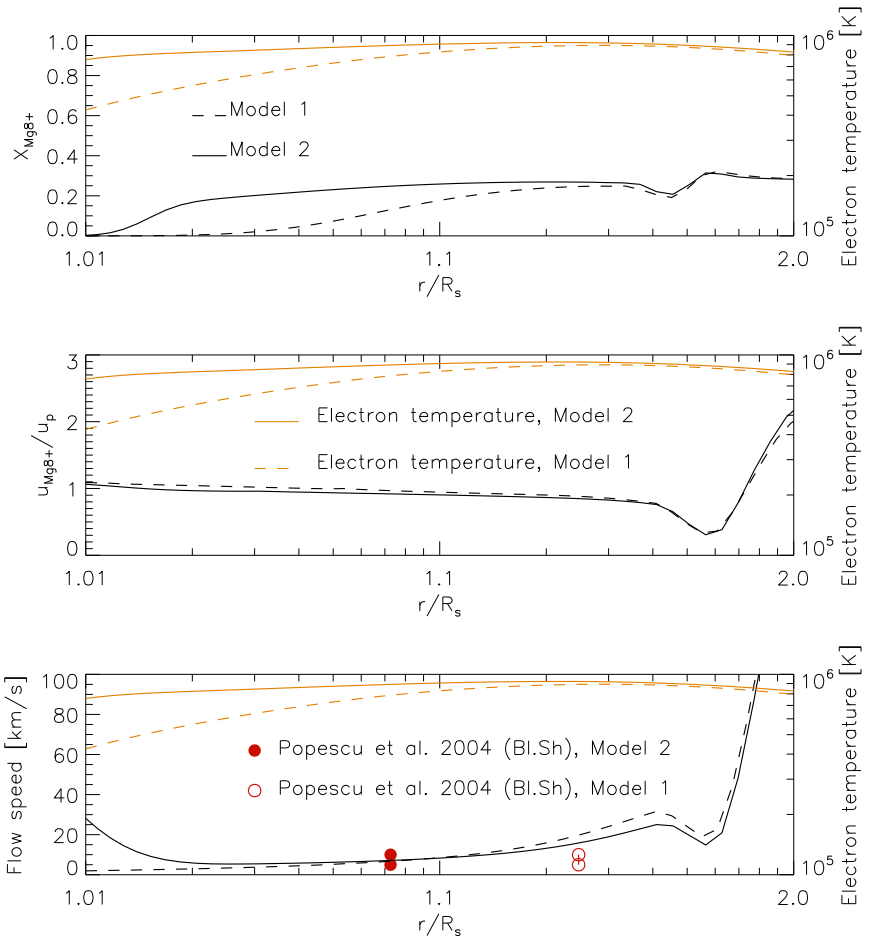

Figure 5.9: Mg^{8+} ion fraction (top panel), $u_{Mg^{8+}}/u_p$ (middle panel) and Mg^{8+} outflow velocity (bottom panel), plotted vs. radial distance from the solar center, Model 1,2.

Chapter 6

Discussion

6.1 Relative flow velocity between minor ions and protons

In the transition region, the differences in density, temperature and flow velocity between the two background models, which arise as a result of the very different flow tube geometries applied, are very large. In spite of this, the degree of coupling to the background for the minor ions, varies very little between the two. For Model 1 (set 1), the relative flow velocity between minor ions and protons, in the formation region of the minor ions, is less than 40% of the proton flow velocity for C^{3+}, O^{3+}, O^{4+}, O^{5+} and Ne^{7+}. For Model 2 (set 1), the relative flow velocity is less than 20% of the proton flow velocity for these ions, i.e. the coupling to the background is somewhat better than for Model 1.

	Model 1, (Set 1)	Model 2, (Set 1)
$u_{C^{3+}}/u_p$	1.15-1.35	1.0
$u_{O^{3+}}/u_p$	1.15-1.25	1.0
$u_{O^{4+}}/u_p$	1.15-1.2	1.0-1.1
$u_{O^{5+}}/u_p$	1.1-1.2	1.0-1.2
$u_{Ne^{7+}}/u_p$	0.9-1.1	0.9-1.1

Table 6.1: Flow speed ratio with protons in the region of maximum ion fraction for C^{3+}, O^{3+}, O^{4+}, O^{5+} and Ne^{7+}, for the two background models.

In table 6.1, we have listed the flow speed ratio with protons in the region of maximum ion fraction for C^{3+}, O^{3+}, O^{4+}, O^{5+} and Ne^{7+}, and for both background models. The ion fraction of Mg^{8+} freezes at its maximum value, of about 0.27, and the flow speed ratio with protons in the region of maximum ion fraction for this ion varies between 0.3 and 2.5. Of the ions in table 6.1, C^{3+} has the largest relative flow velocity with the background, with a flow speed ratio with protons of about 1.3 at the point of

maximum ion fraction in Model 1. However, the flow velocity of the C^{3+} ions has not been observed to exceed 10 km/s. A flow velocity of less than 10 km/s for C^{3+}, and a flow speed ratio with protons of 1.4, would result in a relative flow velocity with protons of less than 2.9 km/s. Measurements of the LOS velocity usually have an accuracy in the range 1-3 km/s (*Xia et al.*, 2003; *Tu et al.*, 2005; *Peter and Judge*, 1999). When the outflow velocity is estimated, based on the measurement of the LOS velocity, further uncertainties are introduced, as assumptions of the magnetic field geometry are made. Thus, the relative flow velocity between the minor ions and the background is within observational uncertainties, even for the ions with the weakest coupling to the background.

All the ions in table 6.1 have well defined ion fraction maxima, with a half-width corresponding to a height range of less than $0.06R_{\odot}$. However, in regions of large density gradients, like the transition region, the region of maximum absolute density (e.g. $(n_{O^{5+}})_{max}$) does not necessarily coincide with the region of maximum ion fraction (e.g. $(x_{O^{5+}})_{max}$). In addition, the excitation rates depend on the electron density, which also decreases with increasing distance from the sun. As a result of the rapid decline of both electron- and minor ion densities in the transition region, the source region of a minor ion emission line may be shifted towards lower temperatures compared to the formation temperature. On the other hand, the rapid decline in density makes it rather unlikely that the region above the ion fraction maximum makes a significant contribution to the emission line. Since the region of maximum ion fraction for the minor ions in table 6.1 corresponds to a relatively narrow height range, we expect that for these ions, the Doppler-shift of the spectral line will reflect the velocity of the ions in the region of maximum ion fraction, however, this should be confirmed through a calculation of the spectral emission profiles.

For Mg^{8+}, the ion fraction increases from zero, at $1.01R_{\odot}$, to about 0.27, at $1.7R_{\odot}$, where it freezes. This means that the radiation from Mg^{8+} comes from a more extended height region, and we cannot exclude the possibility that the region of high outflow velocity, above $1.7R_{\odot}$ makes a contribution to the Doppler-shift of the spectral line. In the case of Mg^{8+}, it is therefore not meaningful to compare the velocity in the region of maximum ion fraction with the observations. To make a comparison with observations we must compute the spectral emission profile of Mg^{8+}, and compare the calculated Doppler velocity with the observed blue-shift.

6.2 Comparison with observed outflow velocities

Table 6.2 compares the estimated outflow/measured blue-shift for C^{3+}, O^{3+}, O^{4+}, O^{5+} and Ne^{7+}, with the calculated outflow velocities at the formation temperatures obtained with Model 1 and Model 2. Also listed are the

formation temperatures obtained by assuming ionization equilibrium (listed in table 3.1) and the formation temperatures obtained with Model 1 and Model 2. The largest discrepancies are found in Model 2, where the calculated outflow velocities of C^{3+}, O^{3+}, O^{4+} and O^{5+} are 30-50 km/s higher than the observed outflow velocities. These large velocities are attributable to the extreme expansion of the flow tube in Model 2 in the region close to the sun. In chapter 7 we have also plotted the estimated outflow/measured blue-shift at the formation temperatures obtained in Model 1 and Model 2, together with the calculated proton outflow velocities for the two models (figure 7.1). In this figure we can see very clearly that Model 1 provides the best overall fit to the observations, however, for Ne^{7+}, the calculated outflow velocity in Model 2 is in better agreement with the observed values.

Ion		Outflow/blue-shift [km/s] T_{form} [10^5K], from table 3.1	Model 1, (Set 1)	Model 2, (Set 1)
C^{3+}	Velocity	0-7	0.5	34
	T_{form}	0.94	1.1	3
O^{3+}	Velocity	0	0.6	33
	T_{form}	1.47	1.5	2.9
O^{4+}	Velocity	0	1	53
	T_{form}	2.22	2.3	4.9
O^{5+}	Velocity	0-10	1.4	44
	T_{form}	2.78	3.1	7.1
Ne^{7+}	Velocity	3-20	3.8	7.5
	T_{form}	6.4	6.4	8.1

Table 6.2: Comparison of observed vs. calculated outflow velocities and ionization equilibrium vs.calculated formation temperatures for C^{3+}, O^{3+}, O^{4+}, O^{5+} and Ne^{7+}, for the two background models.

The formation temperatures in Model 2 are significantly higher than the ionization equilibrium formation temperatures for all the ions in table 6.2. The largest deviation from ionization equilibrium in Model 2 is found for O^{5+}, where the formation temperature is shifted by $4.3 \cdot 10^5$K. For Ne^{7+}, the only ion whose calculated outflow velocity falls within the range of observed outflow velocities in Model 2, the formation temperature is shifted by $1.7 \cdot 10^5$K compared to ionization equilibrium. This corresponds to a shift in height of $0.01 R_\odot$. For Model 1, the maximum deviation from ionization equilibrium in the calculated formation temperatures, for the ions in table 6.2, is about 10%.

When assuming ionization equilibrium, the ion fraction maximum for Mg^{8+} occurs below the temperature maximum. In Model 1 and Model 2 this is not the case (see figure 5.9). Thus, we find that there is a shift in the Mg^{8+} formation temperature as well, relative to the formation temperature

obtained by assuming ionization equilibrium.

6.3 The effect of changing the heating rates

In the previous section, we saw that for Ne^{7+} in Model 2, and for C^{3+}, O^{5+} and Ne^{7+} in Model 1, the calculated outflow velocities are lower than some of the observed outflow velocities. The only way to increase the calculated outflow velocities, without changing the background model, is to increase the heating rates. In the simulations for Ne^{7+}, for Model 2, we found that the outflow velocity of Ne^{7+} in the transition region could only be increased by applying very large heating rates. According to the results obtained in section 5.2.2, the minimum amount of energy that must be deposited in the formation region of Ne^{7+} in order to increase the outflow velocity here is about $40 \cdot 10^{-18}$J/s in the parallel direction and $120 \cdot 10^{-18}$J/s in the perpendicular direction. These are rather extreme heating rates, compared to the heating rates applied for oxygen, which gave outflow velocities and temperatures for O^{5+} that are consistent with observations. By calculating the expansional- and collisional timescales we can show that the degree of coupling to the background plasma, and the outflow velocity in the transition region, remains virtually unchanged for a very large range of minor ion heating rates for all the ions we have studied, and for both the background models.
The timescale for collisions between an ion of species s, and protons (p), is given by

$$\tau_{coll} = \frac{1}{\nu_{sp}}, \tag{6.1}$$

where ν_{st} is defined in equation 4.12. The collisional timescale can be increased by increasing the minor ion temperature.
The expansion timescale for an ion of species s, is given by

$$\tau_{exp} = \left| \frac{n_p}{u_s} \left(\frac{\partial n_p}{\partial r} \right)^{-1} \right|, \tag{6.2}$$

and is the time it takes for the ions to travel through one scale height of proton density. The timescale for expansion is inversely proportional to the flow velocity of the minor species, and can be lowered by increasing their flow speed. In section 4.1, we used the total hydrogen density, i.e. $n_H + n_p$, in the expression for the expansion timescale. In this chapter we are interested in the coupling of the minor ions to the protons, and therefore we use only the proton density in the expression for the expansion timescale. Also, the hydrogen density, in the region that we are interested in ($10^5\text{K} \leq T_e \leq 10^6\text{K}$), is very low compared to the proton density.

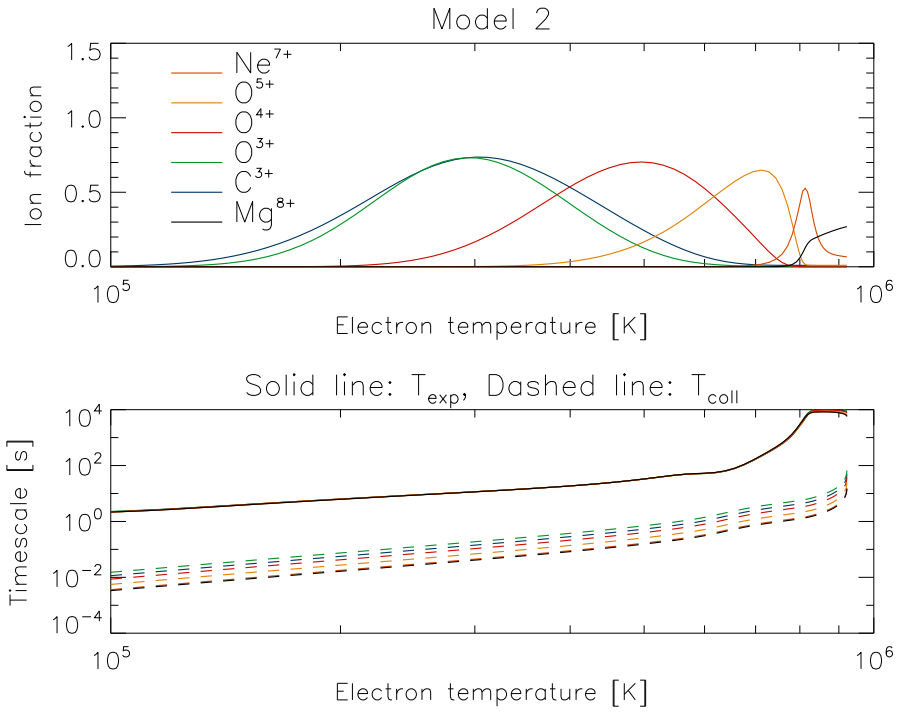

Figure 6.1: Ion fractions (top panel), and expansion (solid lines) and collisional (dashed lines) timescales (bottom panel) in the transition region for all the ions, plotted vs. electron temperature in the range 10^4K to 10^5K, Model 2 (Set 1).

When the timescale for expansion becomes lower than the timescale for collisions, the minor ion species is decoupled from the background plasma. In the region where the timescale for expansion is much higher than the timescale for collisions, moderate heating rates have no effect on the minor ion flow velocity, and the degree of coupling to the background depends solely on the timescale for collisions. When the timescale for collisions is low, corresponding to a high collision frequency, the frictional force (see equation 4.9, section 4.1) can become very large, and thereby able to balance even very large forces, while still retaining a relatively low differential flow velocity with the protons. If we deposit very large amounts of heat in this region, the minor ion flow velocity will eventually increase such that the timescale for expansion becomes lower than the timescale for collisions, and the minor ions decouple from the background. In the region where the minor ion species is decoupled from the background, the heating rates are crucial in determining their flow velocities.

Figure 6.1 shows the ion fractions, and the collisional and expansional timescales in the transition region for $C^{3+}, O^{3+}, O^{4+}, O^{5+}, Ne^{7+}$ and Mg^{8+},

as a function of electron temperature in the range 10^5K to 10^6K. Although the minor ion flow velocities are high throughout most of this temperature range, the timescales for collisions are everywhere lower than the expansion timescales by more than one order of magnitude. The timescales for expansion are larger for Model 1 than for Model 2 in this temperature range. This is because the flow velocity in Model 1 is lower here. The timescales for collisions are also slightly larger for Model 1. Near the electron temperature maximum, the collisional timescales begin to increase rapidly. The timescales for collisions exceed the timescales for expansion, just above the electron temperature maximum.

The difference between the collisional and expansional timescales in the transition region is more or less the same for all the ions in Model 2. In Model 1, this difference is even greater, meaning that in Model 1, larger heating rates are needed to decouple the minor ions from the background in the transition region. This means that the flow velocities of these ions, in the transition region, remains unchanged for a very large range of heating rates, for both background models. There are other constraints on the heating parameters for these ions as well. For oxygen, we saw that the heat should be deposited above the electron temperature maximum, at $1.4R_\odot$ or $1.5R_\odot$, to obtain outflow velocities and temperatures for O^{5+} that are consistent with observations. Therefore, the heating rates cannot affect the flow velocity of O^{5+} in the transition region. Another constraint is put on the heating rates by the ion fractions. The results from Ne^{7+} indicate that the charge states that are dominant in the region where the minor ions decouple from the background are also the dominant charge states in the solar wind far from the sun, although the freezing in distance does not always coincide with the decoupling distance. The ion fractions of C^{3+}, O^{3+}, O^{4+} and O^{5+} are all negligible in the solar wind. (e.g. *Wimmer-Schweingruber et al.*, 1998; *Ko et al.*, 1997) We have not found any published results on observations of the ion fraction of Ne^{7+} in the solar wind. The reason why the decoupling distance does not necessarily coincide with the freezing in distance is that the collision frequency of a minor ion with electrons, which is crucial in the determination of the freezing in distance, is not identical to the collision frequency with protons, which is important in the determination of the decoupling distance.

As we have mentioned earlier, the Doppler shift in the Mg IX emission line far from the sun may have a contribution from the region of high outflow above $1.7R_\odot$. This is probably not the case for the other ions we have investigated. A consequence of this may be that the blue-shift in the emission line of Mg^{8+} far from the sun, contrary to the other ions we have considered, will respond to moderate changes in the heating parameters for Mg^{8+}, which mainly affects the outflow velocity in the region above the temperature maximum.

6.4 The atomic data

As we can see from table 3.1, the formation temperatures of the ions vary quite much depending on which set of atomic data is used in the calculation. The atomic data set used in the numerical model (HAOS-DIAPER (*Judge and Meisner*, 1994)) gives the lowest formation temperatures for all ions except Ne^{7+}.

A change in the formation temperature of an ion means that the ion fraction peak will also move to a different height, and thus it might lead to a change in the calculated Doppler-shift of the spectral emission profile. This could be important, especially for Model 2, where there is a large peak in the flow velocity in the transition region. For the ions that are formed here (C^{3+}, O^{3+}, O^{4+} and O^{5+}), a small change in the formation temperature might move the ion fraction peak into a region of much lower, or much higher outflow. For a more moderate, background model, with a lower outflow velocity in this region, the effects of choosing a different atomic data set is likely to become smaller. However, we cannot exclude the possibility that the choice of atomic data might be of some importance even for a moderate flow tube geometry. The effect of higher formation temperatures would also be of particular importance for Mg^{8+}. For this ion, a higher formation temperature would probably result in a lower ion fraction at the freezing in distance, which again might reduce the contribution from the region of high outflow, above $1.7R_{\odot}$, to the dopplershift of the Mg IX spectral line.

Chapter 7

Conclusions

We have calculated outflow velocities in the transition region and corona for six different minor ions, and two background models. The two background models, primarily characterized by their flow geometry, provides very different solutions for the solar wind in the transition region. The first background model, Model 1, with a moderate expansion, shows low outflow velocities, of order 0-5 km/s, throughout most of the transition region, increasing to about 10-20 km/s in the upper transition region and lower corona. The second background model, Model 2, with a very large expansion, shows high outflow velocities in the middle transition region, of about 30-60 km/s, decreasing to values similar to those in Model 1 in the upper transition region and lower corona. We have found that, for low to moderate heating rates, the flow velocities of $C^{3+}, O^{3+}, O^{4+}, O^{5+}$ and Ne^{7+} deviate with less than 40% from the proton flow velocity in the regions where these ions are the dominant charge states. If we take into concideration the range of velocities that have been observed for these ions, the differential flow velocity with protons falls within the range of observational uncertainties. We also find that these five ions all have well defined ion fraction maxima, with a half-width corresponding to a height range of less than $0.06R_{\odot}$, and we expect that the radiation emitted by these ions mainly stems from the region of maximum ion fraction. This could be confirmed by calculating the spectral emission profiles for these ions. This means that observations of the Doppler-shift of the ionic emission lines from these ions reflect the outflow velocity of the background solar wind in the transition region quite well. The coupling to the background is a little better for Model 2 than for Model 1. For Mg^{8+}, we find that the ion fraction, $n_{Mg^{8+}}/n_{Mg}$, has no well defined maximum, and freezes at a value of 0.27 at $1.7R_{\odot}$. Above this height, the outflow velocity of Mg^{8+} increases, and it is uncoupled from the background solar wind. This means that the radiation from Mg^{8+} might stem from a more extended region in the solar atmosphere and that this ion might not be coupled to the background in the source region of its ionic emission line.

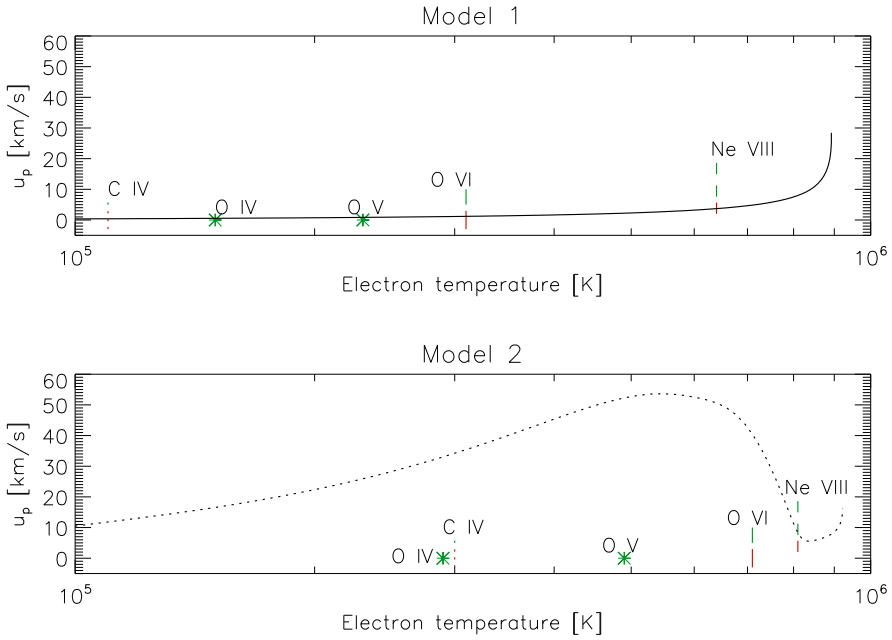

Figure 7.1: Range of estimated outflow velocities and measured blue-shifts (see also figure 3.1), at the formation temperatures obtained with the two background models, for $C^{3+}, O^{3+}, O^{4+}, O^{5+}$ and Ne^{7+}, together with the calculated proton outflow velocities for Model 1 (top panel) and Model 2 (bottom panel).

By calculating the spectral emission profile for this ion we can determine the significance of the contribution from the region of high outflow above $1.7R_{\odot}$, to the Doppler-shift in the Mg IX emission line.

There are significant discrepancies between the calculated and observed outflow velocities for several ions, and for both background models. The calculated outflow velocities can be changed by increasing the amount of energy deposited in the minor ions in the formation region, or by changing the background model. By calculating the collisional and expansional timescales, we have shown that, for a very large range of heating rates, the outflow velocity in the transition region, for all six ions, is unaffected by heating, and depends only on the proton outflow velocity and the degree of coupling to the protons. We have also found indications that observations of the charge state densities of oxygen and carbon in-situ, are inconsistent with large heating rates in the formation region of C^{3+}, O^{3+}, O^{4+} and O^{5+}. In figure 7.1 we have shown the range of estimated outflow velocities and measured blue-shifts, at the formation temperatures obtained with the two background models, for each ion (except Mg^{8+}, since this ion has no well

defined ion fraction maximum). Also shown are the calculated proton outflow velocities. In this figure we clearly see that Model 1 provides the best fit to the observed values, and that the discrepancies are very large for Model 2, where the calculated outflow velocities are generally too high, as a result of the extreme expansion of the flow tube in the transition region. We believe that a funnel-type background model, with a low initial expansion, in contrast to the extremely high initial expansion applied in Model 2, might be able to reproduce both the low outflow velocities seen in the C IV and oxygen lines, as well as the high outflow velocities seen in the Ne VIII line.

For Model 1, the shift in formation temperature for $C^{3+}, O^{3+}, O^{4+}, O^{5+}$ and Ne^{7+}, relative to the ionization equilibrium formation temperature, is negligible. For Model 2, the shift in formation temperature for C^{3+}, O^{3+}, O^{4+}, O^{5+} and Ne^{7+}, relative to the ionization equilibrium formation temperature, is larger, and corresponds to a shift in height of $0.01 R_{\odot}$, for Ne^{7+}, and less than $5 \cdot 10^{-3} R_{\odot}$ for the other ions. For Mg^{8+}, there is also a shift in the formation temperature, both for Model 1 and Model 2, but since the ion fraction of Mg^{8+} freezes before the ion fraction maximum is reached, it is difficult to say how large the shift in formation temperature is for this ion.

Bibliography

NASA/Marshall Solar Physics web site, http://solarscience.msfc.nasa.gov/corona.shtml.

Alazraki, G., and P. Couturier, Solar wind acceleration caused by the gradient of alfven wave pressure, *Astronomy and Astrophysics*, *13*, 380, 1971.

Antonucci, E., G. Noci, J. L. Kohl, G. Tondello, M. C. E. Huber, S. Giordano, C. Benna, A. Ciaravella, S. Fineschi, L. D. Gardner, R. Martin, J. Michels, G. Naletto, P. Nicolosi, A. Panasyuk, C. J. Raymond, M. Romoli, D. Spadaro, L. Strachan, and A. van Ballegooijen, First Results from UVCS: Dynamics of the Extended Corona, *ASP Conf. Ser. 118: 1st Advances in Solar Physics Euroconference. Advances in Physics of Sunspots*, 273–+, 1997.

Antonucci, E., S. Giordano, and M. A. Dodero, Hydrogen and Oxygen Temperatures in Coronal Holes, *Advances in Space Research*, *25*, 1923–1926, 2000.

Antonucci, E., M. A. Dodero, S. Giordano, V. Krishnakumar, and G. Noci, Spectroscopic measurement of the plasma electron density and outflow velocity in a polar coronal hole, *Astronomy and Astrophysics*, *416*, 749–758, 2004.

Belcher, J.W, Alfvenic wave pressures and the solar wind, *The Astrophysical Journal*, *168*, 509, 1971.

Belcher, J.W., and L. Davis Jr., Large amplitude alfven waves in the interplanetary medium, *Journal of Geophysical Research*, *76*, 3534, 1971.

Bell, B., and G. Noci, Intensity of the Fe XV emission line corona, the level of geomagnetic activity, and the velocity of the solar wind, *Journal of Geophysical Research*, *81*, 4508–4516, 1976.

Burlaga, L. F., and K. W. Ogilvie, Heating of the Solar Wind, *The Astrophysical Journal*, *159*, 659–+, 1970.

Chapman, S., The Viscosity and Thermal Conductivity of a Completely Ionized Gas., *The Astrophysical Journal*, *120*, 151–+, 1954.

Cranmer, S. R., Coronal Heating Versus Solar Wind Acceleration, *ESA SP-575: SOHO 15 Coronal Heating*, vol. 15, 154–+, 2004.

Cranmer, S. R., J. L. Kohl, G. Noci, E. Antonucci, G. Tondello, M. C. E. Huber, L. Strachan, A. V. Panasyuk, L. D. Gardner, M. Romoli, S. Fineschi, D. Dobrzycka, J. C. Raymond, P. Nicolosi, O. H. W. Siegmund, D. Spadaro, C. Benna, A. Ciaravella, S. Giordano, S. R. Habbal, M. Karovska, X. Li, R. Martin, J. G. Michels, A. Modigliani, G. Naletto, R. H. O'Neal, C. Pernechele, G. Poletto, P. L. Smith, and R. M. Suleiman, An Empirical Model of a Polar Coronal Hole at Solar Minimum, *The Astrophysical Journal*, *511*, 481–501, 1999.

Cranmer, S. R., J. L. Kohl, M. Miralles, and A. V. Panasyuk, Plasma Conditions in Polar Plumes and Interplume Regions in Polar Coronal Holes, *AGU Spring Meeting Abstracts*, pp. 41–+, 2001.

Dammasch, I. E., K. Wilhelm, W. Curdt, and D. M. Hassler, The NE BT VIII (lambda 770) resonance line: solar wavelengths determined by SUMER on SOHO, *Astronmy and Astrophysics*, *346*, 285–294, 1999*a*.

Dammasch, I.E, D.M Hassler, W. Curdt, and K. Wilhelm, Statistical analysis of euv and uv lines inside and outside of solar coronal holes, *Space Science Reviews*, *87*, 161, 1999*b*.

David, C., A. H. Gabriel, F. Bely-Dubau, A. Fludra, P. Lemaire, and K. Wilhelm, Measurement of the electron temperature gradient in a solar coronal hole, *Astronomy and Astrophysics*, *336*, L90–L94, 1998.

Deforest, C. E., J. T. Hoeksema, J. B. Gurman, B. J. Thompson, S. P. Plunkett, R. Howard, R. C. Harrison, and D. M. Hasslerz, Polar Plume Anatomy: Results of a Coordinated Observation, *Solar Physics*, *175*, 393–410, 1997.

DeForest, C. E., P. L. Lamy, and A. Llebaria, Solar Polar Plume Lifetime and Coronal Hole Expansion: Determination from Long-Term Observations, *The Astrophysical Journal*, *560*, 490–498, 2001.

Del Zanna, G., SOHO CDS observations of coronal hole plumes, *Memorie della Societa Astronomica Italiana*, *74*, 741–+, 2003.

Del Zanna, G., B. J. I. Bromage, and H. E. Mason, Spectroscopic characteristics of polar plumes, *Astronomy and Astrophysics*, *398*, 743–761, 2003.

Doyle, J.G., F.P. Keenan, R.S.I. Ryans, K.M Aggarwal, and A. Fludra, Electron densities above a polar coronal hole based on improved si ix density diagnostics., *Solar Physics*, *188*, 73, 1999.

Dupree, A. K., M. J. Penn, and H. P. Jones, He i 10830 Angstrom Wing Asymmetry in Polar Coronal Holes: Evidence for Radial Outflows, *Astrophysical Journal Letters*, *467*, L121+, 1996.

Esser, R., S. Fineschi, D. Dobrzycka, S. R. Habbal, R. J. Edgar, J. C. Raymond, J. L. Kohl, and M. Guhathakurta, Plasma Properties in Coronal Holes Derived from Measurements of Minor Ion Spectral Lines and Polarized White Light Intensity, *Astrophysical Journal Letters*, *510*, L63–L67, 1999.

Esser, R., Ø. Lie-Svendsen, Å. M. Janse, and M. A. Killie, Solar Wind from Coronal Funnels and Transition Region Lyα, *Astrophysical journal*, *629*, L61–L64, 2005.

Fisher, R., and M. Guhathakurta, Physical Properties of Polar Coronal Rays and Holes as Observed with the SPARTAN 201-01 Coronagraph, *Astrophysical Journal Letters*, *447*, L139+, 1995.

Frazin, R. A., S. R. Cranmer, and J. L. Kohl, Empirically Determined Anisotropic Velocity Distributions and Outflows of O^{5+} Ions in a Coronal Streamer at Solar Minimum, *The Astrophysical Journal*, *597*, 1145–1157, 2003.

Gabriel, A. H., F. Bely-Dubau, and P. Lemaire, The Contribution of Polar Plumes to the Fast Solar Wind, *The Astrophysical Journal*, *589*, 623–634, 2003.

Gabriel, A. H., F. Bely-Dubau, P. Lemaire, and E. Antonucci, Outflow Velocities in Polar Coronal Holes, *IAU Symposium*, 635–+, 2004.

Gabriel, A. H., L. Abbo, F. Bely-Dubau, A. Llebaria, and E. Antonucci, Solar Wind Outflow in Polar Plumes from 1.05 to 2.4 R_{solar}, *The Astrophysical Journal*, *635*, L185–L188, 2005.

Gabriel, A.H, A magnetic model of the solar transition region, *Philosphical transactions of the Royal Society*, *281*, 339, 1976.

Giordano, S., E. Antonucci, G. Noci, M. Romoli, and J. L. Kohl, Identification of the Coronal Sources of the Fast Solar Wind, *The Astrophysical Journal*, *531*, L79–L82, 2000.

Gosling, J. T., Physical Nature of the Low-Speed Solar Wind, *AIP Conf. Proc. 385: Robotic Exploration Close to the Sun: Scientific Basis*, 17–+, 1997.

Gosling, J. T., S. J. Bame, W. C. Feldman, D. J. McComas, J. L. Phillips, B. Goldstein, M. Neugebauer, J. Burkepile, A. J. Hundhausen, and L. Acton, The band of solar wind variability at low heliographic latitudes near

solar activity minimum: Plasma results from the Ulysses rapid latitude scan, *Geophysical Research Letters*, *22*, 3329–3332, 1995.

Guhathakurta, M., T. E. Holzer, and R. M. MacQueen, The Large-Scale Density Structure of the Solar Corona and the Heliospheric Current Sheet, *The Astrophysical Journal*, *458*, 817–+, 1996.

Guhathakurta, M., A. Fludra, S. E. Gibson, D. Biesecker, and R. Fisher, Physical properties of a coronal hole from a coronal diagnostic spectrometer, Mauna Loa Coronagraph, and LASCO observations during the Whole Sun Month, *Journal of Geophysical Research*, *104*, 9801–9808, 1999.

Hansteen, V. H., and E. Leer, Coronal heating, densities, and temperatures and solar wind acceleration, *Journal of Geophysical Research*, *100*, 21577–21594, 1995.

Hartle, R.E, and P.A Sturrock, Two-fluid model of the solar wind, *The Astrophysical Journal*, *151*, 1155, 1968.

Harvey, J. W., Coronal Polar Rays and Polar Magnetic Fields., *The Astrophysical Journal*, *141*, 832–+, 1965.

Harvey, K. L., Coronal structures deduced from photospheric magnetic field and he i λ 10830 observations, *Solar Wind Eight*, 9, 1996.

Hassler, D.M, K. Wilhelm, P. Lemaire, and U. Schüle, Observations of polar plumes with the sumer instrument on soho, *Solar Physics*, *175*, 375, 1997.

Hassler, D.M, I.E. Dammasch, P. Lemaire, P. Brekke, W. Curdt, H.E Mason, J-C. Vial, and K. Wilhelm, Solar wind outflow and the chromospheric magnetic network, *Science Magazine*, *283*, 810, 1999.

Hollweg, J.V., Alfven waves in a two-fluid model of the solar wind, *The Astrophysical Journal*, *181*, 547, 1973.

Hollweg, J.V., Some physical processes in the solar wind, *Reviews of Geophysics*, *16*, 689, 1978.

Hollweg, J.V, Drivers of the solar wind: then and now, *Philosphical transactions of the Royal Society*, *364*, 505, 2006.

Holzer, T. E., Heating and Acceleration of the Solar Plasma (Tutorial Talk), *ESA SP-592: Solar Wind 11/SOHO 16, Connecting Sun and Heliosphere*, vol. 16, 2005.

Janse, Å.M., Ø. Lie-Svendsen, and E. Leer, Describing the flow of fully ionized, magnetized gases: improved gyrotropic transport equations., *Journal of Plasma Physics*, *71*, 611, 2005.

Judge, P. G., and R. W. Meisner, The 'HAO spectral diagnostics package' (HAOS-Diaper), *ESA SP-373: Solar Dynamic Phenomena and Solar Wind Consequences, the Third SOHO Workshop*, vol. 3, 67–+, 1994.

Ko, Y-K., L.A Fisk, J. Geiss, G. Gloeckler, and M. Guhathakurta, An empirical study of the electron temperature and heavy ion velocities in the south polar coronal hole., *Solar Physics*, *171*, 345, 1997.

Kohl, J. L., G. Noci, E. Antonucci, G. Tondello, M. C. E. Huber, L. D. Gardner, P. Nicolosi, L. Strachan, S. Fineschi, J. C. Raymond, M. Romoli, D. Spadaro, A. Panasyuk, O. H. W. Siegmund, C. Benna, A. Ciaravella, S. R. Cranmer, S. Giordano, M. Karovska, R. Martin, J. Michels, A. Modigliani, G. Naletto, C. Pernechele, G. Poletto, and P. L. Smith, First Results from the SOHO Ultraviolet Coronagraph Spectrometer, *Solar Physics*, *175*, 613–644, 1997.

Kohl, J. L., G. Noci, E. Antonucci, G. Tondello, M. C. E. Huber, S. R. Cranmer, L. Strachan, A. V. Panasyuk, L. D. Gardner, M. Romoli, S. Fineschi, D. Dobrzycka, J. C. Raymond, P. Nicolosi, O. H. W. Siegmund, D. Spadaro, C. Benna, A. Ciaravella, S. Giordano, S. R. Habbal, M. Karovska, X. Li, R. Martin, J. G. Michels, A. Modigliani, G. Naletto, R. H. O'Neal, C. Pernechele, G. Poletto, P. L. Smith, and R. M. Suleiman, UVCS/SOHO Empirical Determinations of Anisotropic Velocity Distributions in the Solar Corona, *Astrophysical Journal Letters*, *501*, L127+, 1998.

Kohl, J. L., R. Esser, S. R. Cranmer, S. Fineschi, L. D. Gardner, A. V. Panasyuk, L. Strachan, R. M. Suleiman, R. A. Frazin, and G. Noci, EUV Spectral Line Profiles in Polar Coronal Holes from 1.3 to 3.0 R_solar, *Astrophysical Journal Letters*, *510*, L59–L62, 1999.

Kohl, J. L., G. Noci, S. R. Cranmer, and J. C. Raymond, Ultraviolet spectroscopy of the extended solar corona, *Astronomy and Astrophysics*, *13*, 31–157, 2006.

Kopp, R.A., and T.E. Holzer, Dynamics of coronal hole regions, steady polytropic flows with multiple critical points, *Solar Physics*, *49*, 43, 1976.

Koutchmy, S., Study of the June 30, 1973 trans-polar coronal hole, *Solar Physics*, *51*, 399–407, 1977.

Landini, M., and B. C. Monsignori Fossi, The X-UV spectrum of thin plasmas, *Astronomy and Astrophysics Supplement Series*, *82*, 229–260, 1990.

Leighton, R. B., R. W. Noyes, and G. W. Simon, Velocity Fields in the Solar Atmosphere. I. Preliminary Report., *The Astrophysical Journal*, *135*, 474–+, 1962.

Lie-Svendsen, Ø., E. Leer, and V. H. Hansteen, A 16-moment solar wind model: From the chromosphere to 1 AU, *Journal of Geophysical Research*, *106*, 8217–8232, 2001.

Lopez, R. E., and J. W. Freeman, Solar wind proton temperature-velocity relationship, *Journal of Geophysical Research*, *91*, 1701–1705, 1986.

Mazzotta, P., G. Mazzitelli, S. Colafrancesco, and N. Vittorio, Ionization balance for optically thin plasmas: Rate coefficients for all atoms and ions of the elements H to NI, *Astronomy and Astrophysics Supplement Series*, *133*, 403–409, 1998.

Miralles, M. P., A. V. Panasyuk, L. Strachan, L. D. Gardner, R. Suleiman, S. R. Cranmer, and J. L. Kohl, Solar Cycle 23: Variation of the Solar Corona in the Ultraviolet from Solar Minimum to Solar Maximum, *ISCS 2001 Symposium: Solar Variability, Climate, and Space Weather. Longmont, Colorado, USA, p. 59.*, 59–+, 2001.

Munro, R. H., and B. V. Jackson, Physical properties of a polar coronal hole from 2 to 5 solar radii, *The Astrophysical Journal*, *213*, 874–+, 1977.

Neugebauer, M., and C. W. Snyder, Mariner 2 Observations of the Solar Wind, 1, Average Properties, *Journal of Geophysical Research*, *71*, 4469–+, 1966.

Newkirk, G. J., and J. Harvey, Coronal Polar Plumes, *Solar Physics*, *3*, 321–+, 1968.

Nordling, C., and J. Österman, *Physics Handbook for Science and Engineering*, Studentlitteratur, Lund, 2004.

Noyes, R. W., and R. B. Leighton, Velocity Fields in the Solar Atmosphere. II. The Oscillatory Field., *The Astrophysical Journal*, *138*, 631–+, 1963.

Parker, E.N., Dynamics of the interplanetary gas and magnetic fields, *The Astrophysical Journal*, *128*, 664, 1958.

Parker, E.N., Dynamical theory of the solar wind, *Space Science Reviews*, *4*, 666, 1965.

Peter, H., Analysis of transition-region emission-line profiles from full-disk scans of the sun using the sumer instrument on soho, *The Astrophysical Journal*, *516*, 490, 1999.

Peter, H., and P.G. Judge, On the doppler shifts of solar ultraviolet emission lines, *The Astrophysical Journal*, *522*, 1148, 1999.

Popescu, M. D., J. G. Doyle, and L. D. Xia, Network boundary origins of fast solar wind seen in the low transition region?, *Astronomy and Astrophysics*, *421*, 339–348, 2004.

Raouafi, N.-E., J. W. Harvey, and S. K. Solanki, Properties of Solar Polar Coronal Plumes Constrained by Ultraviolet Coronagraph Spectrometer Data, *The Astrophysical Journal*, *658*, 643–656, 2007.

Schwenn, R., Large-Scale Structure of the Interplanetary Medium, in *Physics of the Inner Heliosphere*, vol. 1, edited by R. Schwenn and E. Marsch, pp. 99–182, 1990, 1990.

Simon, G. W., and R. B. Leighton, Velocity Fields in the Solar Atmosphere. III. Large-Scale Motions, the Chromospheric Network, and Magnetic Fields., *The Astrophysical Journal*, *140*, 1120–+, 1964.

Steinitz, R., and M. Eyni, Global properties of the solar wind. I - The invariance of the momentum flux density, *The Astrophysical Journal*, *241*, 417–424, 1980.

Stucki, K., S. K. Solanki, I. Rüedi, and U. Schüehle, Relationship between Line Shift and Intensity Inside Coronal Holes, *ESA SP-446: 8th SOHO Workshop: Plasma Dynamics and Diagnostics in the Solar Transition Region and Corona*, vol. 8, 633–+, 1999.

Tu, C.-Y., E. Marsch, K. Wilhelm, and W. Curdt, Ion Temperatures in a Solar Polar Coronal Hole Observed by SUMER on SOHO, *Astrophysical Journal*, *503*, 475–+, 1998.

Tu, C.-Y., E. Marsch, and K. Wilhelm, Ion Temperatures as Observed in a Solar Coronal Hole, *Space Science Reviews*, *87*, 331–334, 1999.

Tu, C-Y., C. Zhou, E. Marsch, L-D. Xia, L. Zhao, J-X. Wang, and K. Wilhelm, Solar wind origin in coronal funnels, *Science Magazine*, *308*, 519, 2005.

von Steiger, R., J. Geiss, G. Gloeckler, and A. B. Galvin, Kinetic Properties of Heavy Ions in the Solar Wind From SWICS/Ulysses, *Space Science Reviews*, *72*, 71–+, 1995.

Wang, Y.-M., Polar plumes and the solar wind, *Astrophysical Journal Letters*, *435*, L153–L156, 1994.

Wang, Y.-M., and N. R. Sheeley Jr., Coronal Plumes and Their Relationship to Network Activity, *The Astrophysical Journal*, *452*, 457–+, 1995.

Wang, Y.-M., N. R. Sheeley Jr., K. P. Dere, R. T. Duffin, R. A. Howard, D. J. Michels, J. D. Moses, J. W. Harvey, D. D. Branston, J.-P. Delaboudiniere, G. E. Artzner, J. F. Hochedez, J. M. Defise, R. C. Catura, J. R. Lemen, J. B. Gurman, W. M. Neupert, J. Newmark, B. Thompson, and A. Maucherat, Association of Extreme-Ultraviolet Imaging Telescope (EIT) Polar Plumes with Mixed-Polarity Magnetic Network, *Astrophysical Journal Letters*, *484*, L75+, 1997.

Wilhelm, K., Solar coronal-hole plasma densities and temperatures, *Astronomy and Astrophysics*, *455*, 697–708, 2006.

Wilhelm, K., E. Marsch, B. N. Dwivedi, D. M. Hassler, P. Lemaire, A. H. Gabriel, and M. C. E. Huber, The Solar Corona above Polar Coronal Holes as Seen by SUMER on SOHO, *The Astrophysical Journal*, *500*, 1023–+, 1998.

Wilhelm, K., I.E. Dammasch, E. Marsch, and D.M. Hassler, On the source regions of the fast solar wind in polar coronal holes, *Astronomy and Astrophysics*, *353*, 749, 2000.

Wimmer-Schweingruber, R. F., R. von Steiger, J. Geiss, G. Gloeckler, F. M. Ipavich, and B. Wilken, O^{5+} in High Speed Solar Wind Streams: SWICS/Ulysses Results, *Space Science Reviews*, *85*, 387–396, 1998.

Woo, R., and S. R. Habbal, Imprint of the Sun on the Solar Wind, *Astrophysical Journal Letters*, *510*, L69–L72, 1999.

Woo, R., S. R. Habbal, R. A. Howard, and C. M. Korendyke, Extension of the Polar Coronal Hole Boundary into Interplanetary space, *The Astrophysical Journal*, *513*, 961–968, 1999.

Xia, L-D., E. Marsch, and W. Curdt, On the outflow in an equatorial coronal hole, *Astronomy and Astrophysics*, *399*, L5, 2003.

Xia, L-D., E. Marsch, and K. Wilhelm, Observations of sumer and mdi on soho, *Astronomy and Astrophysics*, *424*, 1025, 2004.

Zirker, J. B., Coronal holes and high-speed wind streams, *Reviews of Geophysics and Space Physics*, *15*, 257–269, 1977.